Yang, Y, Bashir, M, Michailides, C, Mei, X, Wang, J and Li, C

Coupled Analysis of a 10 MW Multi-Body Floating Offshore Wind Turbine Subjected to Tendon Failures

Coupled Analysis of a 10 MW Multi-Body Floating Offshore Wind Turbine Subjected to Tendon Failures

Yang YANG[a, b], Musa BASHIR [b *], Constantine MICHAILIDES [c], Xuan MEI [d], Jin WANG [b], Chun LI [e]

[a, b] Faculty of Maritime and Transportation, Ningbo University, Ningbo, 315211, P.R. China

[b] Liverpool Logistics, Offshore and Marine (LOOM) Research Institute, School of Engineering, Liverpool John Moores University, Liverpool, Byrom Street, L3 3AF, UK

[c] Department of Civil Engineering and Geometrics, Cyprus University of Technology, Limassol, Saripolou 2-8, 3036, Cyprus

[d] Department of Civil Engineering, Tongji University, Shanghai, 200092, P. R. China

[e] School of Energy and Power Engineering, University of Shanghai for Science and Technology, Shanghai, 200093, P.R. China

Abstract: In this study dynamic responses of a 10 MW offshore wind turbine supported by a multi-body floating platform that consists of a wide cylindrical platform and a cylindrical ballast body suspended by six tendons are analyzed and predicted for different tendon breakage scenarios. A newly-developed and validated fully coupled numerical tool (F2A) based on AQWA and FAST is used to perform aero-hydro-servo-elastic analysis of the floating offshore wind turbine (FOWT). The results indicate that the dynamic behavior of the platform is heavily influenced by the state of tendons health. Roll and yaw motions of the platform under a tendon breakage are found to experience 6 times magnitude amplification of the typical responses, depending on the specific environmental conditions considered. Moreover, the peak tension in the tendon adjacent to the broken tendon experienced an increase of 165% in magnitude. The collective-pitch mode of the platform and wave excitation that are the main contributors to the surge and pitch fluctuations are slightly affected by tendon breakages. The influence of tendon

*Corresponding author: M.B.Bashir@ljmu.ac.uk

breakages is found to be only significant on the local-pitch and coupled-pitch modes of the platform. In addition, multifractal spectra of the platform accelerations under different tendon failure scenarios show distinct fractal characteristics that can effectively identify and diagnose tendon failures, which is essential to the development of a structural health monitoring system of FOWTs.

Keywords: Floating Offshore Wind Turbine; Dynamic Responses; Multi-body Platform; Tendon Failure; Fully Coupled Analysis; F2A;

1 Introduction

Wind energy continues to play a significant role in the uptake of green energy as opposed to fossil fuels that are largely responsible for environmental pollution. Over 50 GW capacity of wind energy was added into global electric grid in 2019 [1-2]. Recently, improving the techniques applicable to design of floating offshore wind turbines (FOWTs) has been the main focus of research in order to further reduce the levelized cost of electricity (LCOE) of wind turbines to a more rational and competitive level.

FOWTs have benefitted from some European Union (EU) funded research on developing platforms for 10 MW-class wind turbines due to their high potentials in reducing LCOE [3-5]. For instance, a semi-submersible concept for the DTU (Technical University of Denmark) 10 MW wind turbine was developed in the INNWIND project [6] and the hydrodynamic performance of the corresponding platform was evaluated. In the LIFES50+ project [7], two semi-submersible concepts, a barge and a Tension Leg Platform (TLP) were developed to support 10 MW FOWTs. HAWC2 and FAST were used to perform fully coupled analysis of the FOWTs after a comprehensive comparison with experimental tests. Most recently, a novel multi-body floating platform, the so-called TELWIND, was developed by ESTEYCO [8] for

10+ MW FOWTs for the ARCWIND project as shown in Fig. 1.

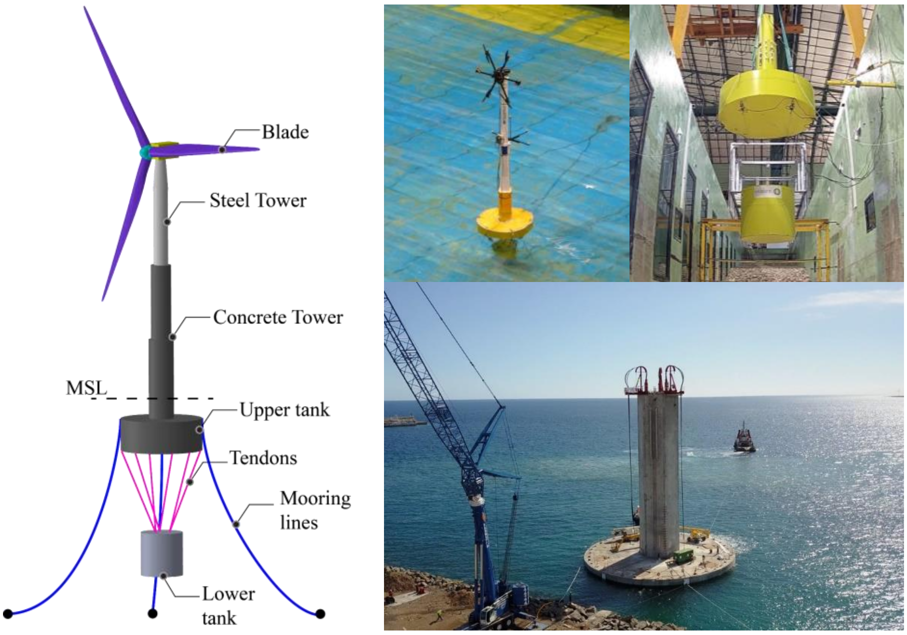

Fig.1： TELWIND platform design concept

The multi-body platform supporting a telescopic tower eases the installation and transportation processes. Moreover, the support system of the FOWT is constructed using concrete material to reduce costs. The upper tank (UT) provides buoyancy while the lower tank (LT) ballasts the platform for stability. As a result, the overall center of gravity (CoG) of the wind turbine system is much lower than the center of buoyancy (CoG), guaranteeing a good roll/pitch motion stability. The low-cost TELWIND platform design is expected to reduce the LCOE of FOWTs to a more competitive level. The TELWIND concept uses six taut tendons to connect the UT with the LT. It is apparent that safety and stability of the TELWIND FOWT significantly depend on the integrity of the tendons. Therefore, the TELWIND concept requires a comprehensive study of its dynamic behavior especially when a tendon failure occurs under multiple loadings. Conducting a failure analysis of the tendons is beneficial in the identification of tendon failures, which is a pre-requisite to developing a robust structural health monitoring system for the multi-body platform and other similar concepts like TLP.

Numerous studies have been conducted to investigate the consequences and impacts of a mooring/tendon breakage on floating platforms. Gao *et al.* [9] investigated the influence of a mooring breakage on the annual extreme tension and fatigue damage of the remaining mooring lines of a TLP. It was found that the extreme tension in the mooring line adjacent to the broken mooring is increased by 20% to 30%. In addition, the breakage of a mooring line produces an increase of 50% to 90% in the fatigue damage of the remaining lines. Zhang *et al.* [10] performed a dynamic analysis of a deep water semi-submersible subjected to a progressive mooring line failure under a hurricane condition. Following the breakage of a mooring line, each of the remaining mooring lines breaks because its tension exceeded the limit of the material strength. Yang *et al.* [11-13] analyzed the transient responses of a hull-tendon-riser coupled TLP model when a tendon is suddenly disconnected by accident. The dynamic behavior of the TLP and transient tensions of the remaining tendons are investigated. Ahmed *et al.* [14] investigated the responses of a truss spar platform modelled as a three degree-of-freedom (DOF) rigid structure after one or two mooring lines are broken for both symmetric and asymmetric mooring configurations. The quasi-static catenary model was used to predict the tension of the mooring lines. Malayjerdi *et al.* [15] compared the dynamic responses of a TLP under intact and damaged tendon conditions. The static stability of the TLP with one or three broken tendons was investigated. Yu *et al.* [16] investigated the effects of a sudden breakage and progressive failure of tendons on the dynamic responses of a TLP coupled with risers. A total failure of the tendon could be caused by a local damage of small magnitude under an extreme sea state. Bae *et al.* [17] investigated the performance changes due to a broken mooring line of a 5 MW semi-submersible FOWT using CHARM3D-FAST. Li *et al.* [18] investigated the transient responses of a spar-type 5 MW FOWT with fractured mooring lines using an in-house simulation tool. A large drift was caused by a mooring failure and the risk of collision between FOWTs was discussed for two different wind farm configurations. However, it is noted that the aerodynamic loads were predicted using a quasi-steady method and the aero-elastic effects of the blades were ignored. Moreover, the memory effects on the free-surface were not examined. Ma *et al.* [19] investigated the dynamic responses of a 5 MW semi-submersible FOWT under a mooring line breakage due to extreme coherent gust using a commercial tool, SIMA. The time length of the extreme gust occurrence was investigated. However, it is noted that a quasi-steady method was used in predicting the aerodynamic loads, implying that the fully coupled aero-hydro-servo-elastic was not well examined.

We have recently investigated various aspects of the proposed TELWIND FOWT concept [20-21]. In one of these studies, F2A, an aero-hydro-servo-elastic coupling framework capable of examining fully coupled responses of multi-body platform concepts, was developed and validated. Furthermore, fatigue damage of the tendons was evaluated for a potential site located off the northern coast of Scotland in the other study. These two studies confirmed the good hydrodynamic performance of the TELWIND concept but raised a problem that the safety and stability of the platform significantly depend on the integrity of the tendons. Therefore, it is imperative to investigate the motion stability of the TELWIND concept when one tendon fails suddenly.

As indicated previously, fully coupled effects between environmental loads and structural elasticity of a FOWT under a tendon/mooring breakage scenario have not been examined adequately. Therefore, this study employs the validated fully coupled tool, F2A, to examine the dynamic responses of the TELWIND FOWT subjected to a tendon breakage. The transient behaviors of the FOWT with intact and broken tendons are investigated for three typical environmental conditions that cover below-rated, rated and over-rated operational states. The platform rotational motions and tension in the remaining tendons under a tendon breakage condition are obtained. The platform stability and safety of the remaining tendons are discussed. In addition, spectral responses based on the Welch transformation and the wavelet leader approaches are obtained in order to provide characteristics corresponding to tendon breakages, which is beneficial to the development of structural health monitoring system for the identification and detection of a tendon damage.

2 Model description of the wind turbine

2.1 DTU 10 MW wind turbine

In the INNWIND project, DTU developed a reference 10 MW wind turbine in collaboration with Vestas. The rotor diameter and hub-height are 178.3 m and 119 m, respectively. Diameter and overhang of the hub are 2.8 m and 7.1 m, respectively. The low speed shaft connecting the rotor and gearbox has an up-tilt angle of 5 degrees. The wind turbine operates in the wind speed range of 4 m/s to 25 m/s for normal power production based on a variable-speed and pitch-to-feather control strategy. The DTU 10 MW wind turbine has been widely used in the development of various offshore support structures. More specifications of the structural properties of the wind turbine can be found in the reference [22].

2.2 The 10 MW TELWIND FOWT platform concept

ESTEYCO developed a novel multi-body platform for 5 MW offshore wind turbines in the TELWIND project. The 5 MW TELWIND platform concept is employed in the ARCWIND project following an up-scaling design for its application and adaptation as 10 MW FOWTs.

The tower, integrated with the platform, is designed as telescopic in order to ease transport and installation processes. To reduce the total cost, the support system of the FOWT, with an exception to the topmost steel-made tower section, are constructed using concrete.

The 10 MW TELWIND platform is applicable to 110 water depth areas or deeper seas with appropriate modifications on mooring lines configuration. A mooring line in this concept has a submerged weight of 250 kg/m and a dry weight of 288 kg/m. The unstretched length of each mooring line is 620 m. The fairleads are distributed uniformly around the UT top surface with an interval angle of 120 degrees. The anchors are placed radially with a diameter of 1200 m.

Fig. 2 illustrates the orientations of the tendons and mooring lines. It is noted that six and three connection points are attached on the UT bottom surface and the LT top surface, respectively. The tendon connection points on the LT are placed radially with a diameter of 9 m and at an interval angle of 120 degrees. Each tendon has a length of 48.81 m and a cross-area of 57,600 mm^2. The diameter of the connection points is identical to the diameter of the tendons.

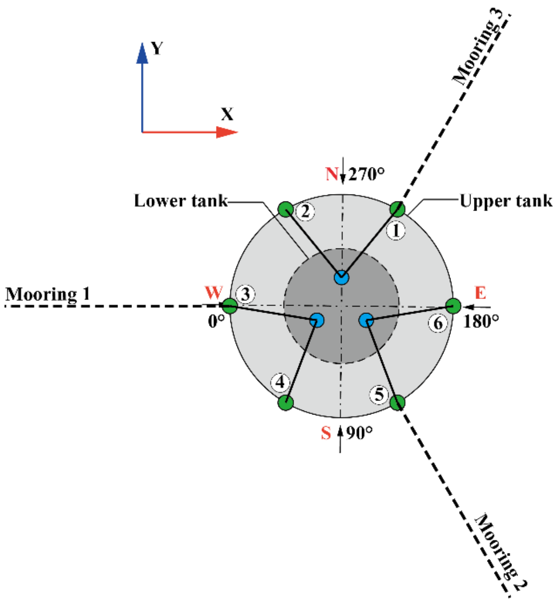

Fig. 2: Orientations of the tendons and mooring lines

By conducting a stability analysis of the moored FOWT, the natural periods, modal shapes and eigenvectors of the multi-body platform are obtained and presented in Table 1. Different from a conventional single-body platform, this particular platform has three pitch modes. Apart from the collective pitch mode, the platform will vibrate in the local-pitch mode and coupled-pitch mode. The eigenvector of the platform is defined as the ratios of the surge amplitudes due to pitch motions to the vertical distance between the UT and LT. In the local-pitch mode, only the LT vibrates at a notable amplitude that is equivalent to 8.3% of the distance between the tanks. Both the tanks vibrate with a notable magnitude but in different directions in the coupled-pitch mode. Due to the symmetry of the platform, the roll modes of the platform are similar to the pitch modes.

Table 1: Natural periods and vibration modes of the platform

Mode description	Collective pitch	Local-pitch	Coupled-pitch
Natural period /(s)	36.53	3.08	1.44
Natural frequency /(Hz)	0.02737	0.32501	0.69224
Eigenvector/[LT, UT]	[-0.052, 0.050]	[-0.083, 0.004]	[-0.061, -0.055]
Vibration modes	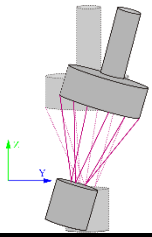	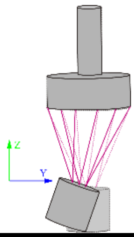	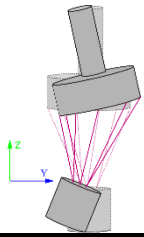

3 Methodology of the coupling framework

The F2A coupling framework [20] is developed by implementing aero-elastic-servo simulation capabilities within the *user_force*64.dll of AQWA. The hydrodynamic loads and mooring restoring forces acting on the floating platform are predicted in AQWA solver. The aerodynamic loads calculated in the DLL are passed into AQWA solver for the determination of platform responses. The platform kinematics are used in calculating the aero-elastic responses of the blades and tower. The subsequent sections present a general description of the methodologies of the coupling framework.

3.1 Aerodynamic and structural modelling

The blade element momentum theory (BEMT) and the generalized dynamic wake (GDW) method are employed to predict aerodynamic loads acting on the rotor [23-24]. Fig. 3 describes the aerodynamic forces on an arbitrary blade element with a length of d*r* [25].

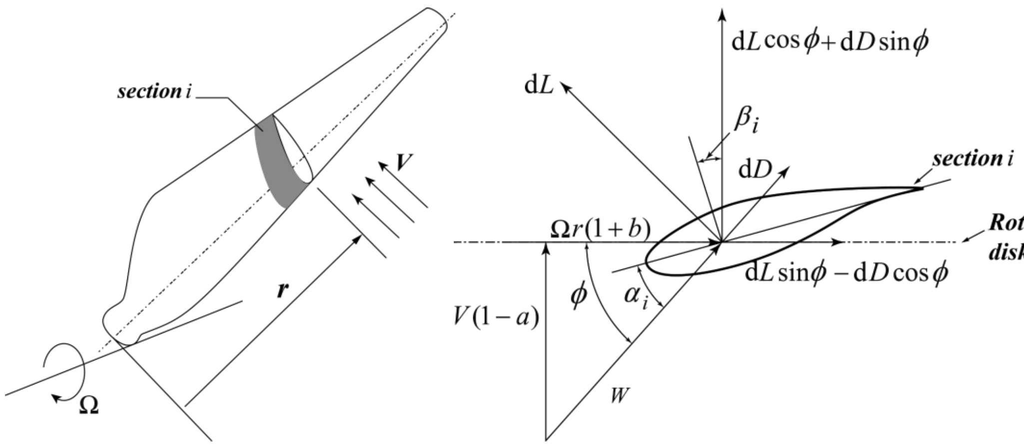

Fig. 3: Velocities and aerodynamic forces of an arbitrary blade section

where Ω is the rotor speed. r is the local radius of the blade element. V and W denote the inflow and absolute speed, respectively. a and b are axial and tangential induction coefficients, respectively. α , β and ϕ are the angles of attack, twist and inflow, respectively. L and D are the lift and drag forces respectively.

For a known induction velocity, the angle of attack will be determined in order to obtain the aerodynamic coefficients of the sectional airfoil. Then, thrust and torque produced by the blade element can be denoted using Eq. (1) and Eq. (2):

$$\mathrm{d}T = \frac{1}{2}\rho W^2 c(C_l \cos\phi + C_d \sin\phi)\mathrm{d}r \tag{1}$$

$$\mathrm{d}M = \frac{1}{2}\rho W^2 c(C_l \sin\phi - C_d \cos\phi)r\mathrm{d}r \tag{2}$$

where C_l and C_d are respectively the lift and drag coefficients of the sectional airfoil. c is the chord length of the blade element.

The GDW method is applied to obtain the distributions of induced velocity and pressure over the rotor disk by solving the Laplace's equation based on potential flow assumptions [26].

Fig. 4 presents the procedure of calculating aerodynamic loads acting on a rotor in AeroDyn. More details of the theory used in AeroDyn for solving the time-dependent governing ordinary differential equations can be found in references [23-24].

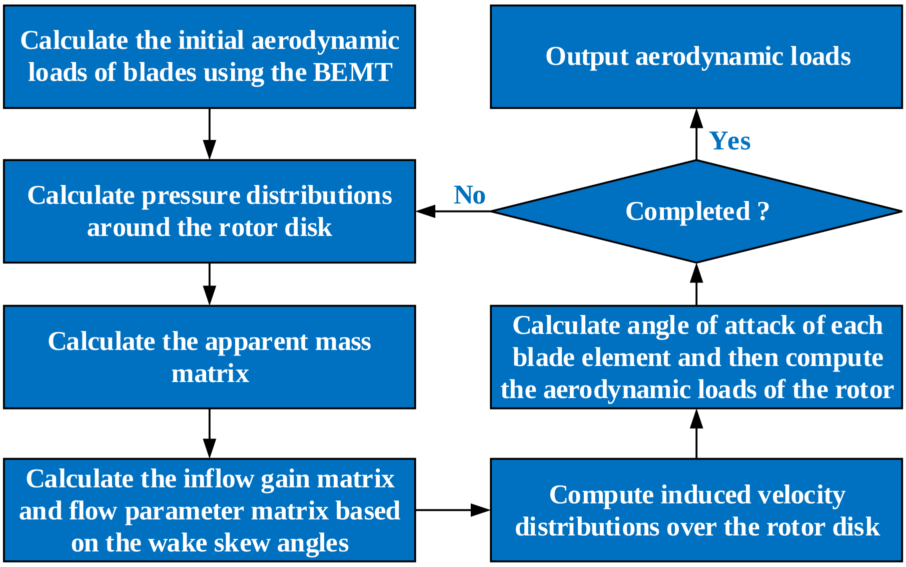

Fig. 4: Flowchart of the process for calculating aerodynamic loads on a rotor

In this study, the blades and tower are modelled as cantilevered beams using the linear modal approach. The first two flapwise and one edgewise modes of each blade are examined. The first two fore-aft and side-side modes of the tower are considered. The equation of motion of the wind turbine is developed using Kane's method as denoted in Eq. (3).

$$\boldsymbol{F}_i^* + \boldsymbol{F}_i = 0 \tag{3}$$

where $\boldsymbol{F}_i^*$ and $\boldsymbol{F}_i$ are the generalized inertia and active forces corresponding to the i^{th} DOF of the wind turbine.

The generalized inertia force of the tower $\boldsymbol{F}_{\text{Twr}}^*$ is denoted as:

$$\boldsymbol{F}_{\mathrm{Twr}}^{*} = -\sum_{i=1}^{N}\int_{0}^{H} \rho_{\mathrm{Twr}}(h)\cdot v_{i,\mathrm{Twr}}(h)\cdot a_{\mathrm{Twr}}(h)\cdot \mathrm{d}h \tag{4}$$

where H is the length of tower; $\rho_{\mathrm{Twr}}(h)$ and $a_{\mathrm{Twr}}(h)$ are mass density and acceleration of the tower, respectively; $v_{i,\mathrm{Twr}}(h)$ is partial velocity of the local tower element contributed by the i^{th} DOF of the wind turbine.

The generalized inertia forces on the blades can be represented in a similar formula. The generalized active force consists of aerodynamic load $F_{i,\mathrm{aero}}$, elastic restoring force $F_{i,\mathrm{elastic}}$, gravitational load $F_{i,\mathrm{grav}}$ and damping force $F_{i,\mathrm{damp}}$, as denoted in Eq. (5).

$$F_i = F_{i,\mathrm{aero}} + F_{i,\mathrm{elastic}} + F_{i,\mathrm{grav}} + F_{i,\mathrm{damp}} \tag{5}$$

The generalized active elastic restoring force of the tower is defined as a partial derivative of the potential energy with respect to the generalized coordinate, as follows:

$$F_{\mathrm{Twr,elastic}} = \frac{\partial V_{\mathrm{PE}}}{\partial q_{\mathrm{Twr}}} = \frac{\partial\left[\frac{1}{2}\sum_{i}^{n}\sum_{j}^{n} k_{ij}\cdot q_i(t)\cdot q_j(t)\right]}{\partial\left[q_{\mathrm{Twr}}(t)\right]} \tag{6}$$

where V_{PE} is the potential energy of the tower; $q_i(t)$ is the generalized coordinate associated with the i^{th} mode pertaining to the tower at the time of t; n is the number of the examined modes of the blade; k_{ij} is the generalized stiffness of the blade and its value is zero when $i \neq j$.

The generalized stiffness of the tower is denoted as:

$$k_{ij} = \int_{0}^{H} EI_{\mathrm{Twr}}(r)\frac{\mathrm{d}^2\varphi_i(h)}{\mathrm{d}h^2}\frac{\mathrm{d}^2\varphi_j(h)}{\mathrm{d}h^2}\mathrm{d}h + k_{\mathrm{tm},ij} + k_{\mathrm{lm},ij} \tag{7}$$

where $EI_{\mathrm{Twr}}(h)$ is the distributed stiffness of the tower. $\varphi_i(h)$ is the i^{th} normalized modal shape of the tower; $k_{\mathrm{tm},ij}$ and $k_{\mathrm{lm},ij}$ are the generalized stiffness due to the top mass and local mass of the tower, as derived in Eq. (8) and Eq. (9), respectively.

$$k_{\mathrm{tm},ij} = -gm_{\mathrm{top}}\int_{0}^{H}\frac{\mathrm{d}\varphi_i(h)}{\mathrm{d}h}\frac{\mathrm{d}\varphi_j(h)}{\mathrm{d}h}\mathrm{d}h \tag{8}$$

$$k_{\mathrm{lm},ij} = -g\int_0^H \rho_{\mathrm{Twr}}\left(h\right)\left[\int_0^h \frac{\mathrm{d}\varphi_i\left(h'\right)}{\mathrm{d}h'}\frac{\mathrm{d}\varphi_j\left(h'\right)}{\mathrm{d}h'}\mathrm{d}h'\right]\mathrm{d}h \tag{9}$$

where g and m_{top} are the gravitational acceleration and tower-top mass, respectively.

3.2 Modelling of mooring system and tendons in AQWA

The mooring lines and tendons are modelled as a dynamic cable using the finite element method. Each cable is discretized into finite elements with their mass concentrated at the centroid of the discretized element. Fig. 5 presents a schematic diagram of the forces on a cable element.

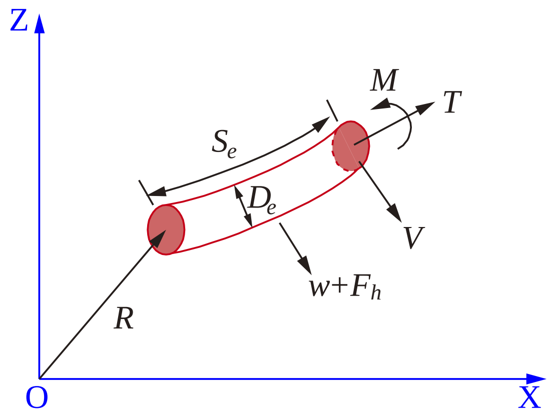

Fig. 5: Forces on a cable element

The equation of motion of the cable element is derived as:

$$\begin{cases} \dfrac{\partial \mathbf{T}}{\partial S_e} + \dfrac{\partial \mathbf{V}}{\partial S_e} + \boldsymbol{w} + \boldsymbol{F}_h = m_e \dfrac{\partial^2 \mathbf{R}}{\partial t^2} \\ \dfrac{\partial \mathbf{M}}{\partial S_e} + \dfrac{\partial \mathbf{R}}{\partial S_e} \times \mathbf{V} + \mathbf{q} = \mathbf{0} \end{cases} \tag{10}$$

where **T** and **V** are, respectively, the tension force and shear force vectors at the first node of the element; **R** is the position vector of the first node of the cable element; S_e is the unstretched length of the element; $\boldsymbol{w}$ and $\boldsymbol{F}_h$ are, respectively, the weight and hydrodynamic load vectors per unit length of the element; m_e is the mass per unit length. **M** is the bending moment vector at the first node of the element; and $\mathbf{q}$ is the distributed moment load per unit length of the element.

The bending moment and tension are denoted as follows:

$$\begin{cases} \mathbf{M} = EI \cdot \dfrac{\partial \mathbf{R}}{\partial S_e} \times \dfrac{\partial^2 \mathbf{R}}{\partial S_e^2} \\ \mathbf{T} = EA \cdot \varepsilon \end{cases} \tag{11}$$

where ε is the stretched length; EI and EA are the bending stiffness and axial stiffness of the cable, respectively. The stiffness of the tendon will be zero if a failure occurs at the specific instant when examining the tendon breakage scenario.

3.3 Development of the coupling framework

The coupling framework is developed within AQWA by implementing the aero-servo-elastic simulation capabilities in the *user_force*64.dll. The fully coupled analysis of the FOWT is performed in AQWA. The DLL is invoked by the AQWA solver to obtain the aerodynamic loads at each time step. The loads obtained by the DLL are fed into the solver to be coupled with the hydrodynamic loads and mooring restoring forces in determining the platform acceleration. The equation of motion of each tank of the multi-body platform is derived as:

$$(\boldsymbol{m} + \boldsymbol{A}_{\mathrm{wv}})\ddot{\boldsymbol{X}}(t) + \boldsymbol{C}\dot{\boldsymbol{X}}(t) + \boldsymbol{K}\boldsymbol{X}(t) + \int_0^t \boldsymbol{h}(t-\tau)\ddot{\boldsymbol{X}}(\tau)\mathrm{d}\tau = \boldsymbol{F}_{\mathrm{h}}(t) + \boldsymbol{F}_{\mathrm{t}}(t) + \boldsymbol{F}_{\mathrm{e}}(t) \tag{12}$$

where $\boldsymbol{m}$ and $\boldsymbol{A}_{\mathrm{wv}}$ are respectively the inertial mass and added mass of the tank; $\boldsymbol{K}$ and $\boldsymbol{C}$ are, respectively, the total stiffness and damping matrices; $\boldsymbol{X}(t)$, $\dot{\boldsymbol{X}}(t)$ and $\ddot{\boldsymbol{X}}(t)$ are, respectively, the displacement, velocity and acceleration vectors of the tank; $\boldsymbol{h}(t)$ is the acceleration impulse function matrix used to examine the radiation memory effects; $\boldsymbol{F}_{\mathrm{h}}(t)$ and $\boldsymbol{F}_{\mathrm{t}}(t)$ are, respectively, the total hydrodynamic and mooring load vectors acting on the tank; $\boldsymbol{F}_{\mathrm{e}}(t)$ is the external force obtained through the DLL.

Fig. 6 presents a schematic diagram of the F2A coupling framework. AeroDyn, ElastDyn and ServoDyn modules of FAST are incorporated within the DLL for solving the equation of motion of the wind turbine excluding the platform's DOFs.

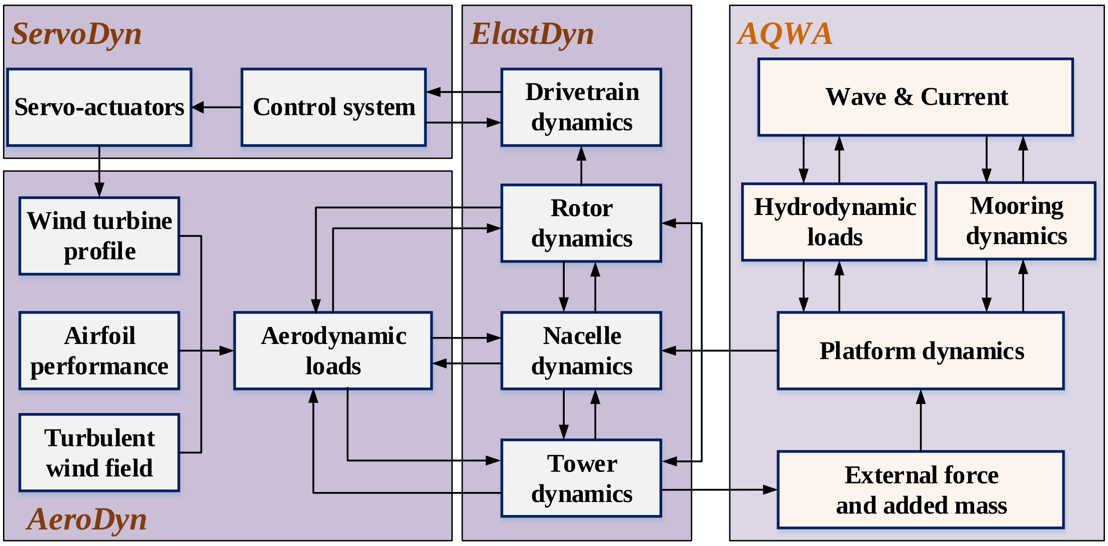

Fig. 6: Schematic diagram of the F2A coupling framework

The procedures of an arbitrary simulation examined using F2A are described to clearly explain the coupling between different components as follows:

(1) The platform responses are passed into ElastDyn through the DLL to update the kinematics of the upper structures including tower, nacelle and blades.

(2) Aerodynamic loads on the rotor and tower are predicted in AeroDyn based on the given wind speed and the current structure velocities.

(3) The structural responses are obtained by solving Eq. (3) in ElastDyn based on the aerodynamic loads and structural kinematics.

(4) The generator speed and blade pitch are adjusted in ServoDyn for normal power production. The control measures will affect the aerodynamic load prediction in the next time step.

(5) The tower-base loads obtained in ElastDyn are fed back to the AQWA program to be combined with the hydrodynamic loads and mooring restoring forces for calculating

the platform responses.

(6) Steps (1)~(5) are repeated until the termination of the simulation.

It is apparent that the platform responses are affected by the dynamic behavior of the wind turbine's upper structures, and vice versa.

The incorporation of FAST to AQWA is implemented by modifying the source code of FAST. The specific modifications to the source code are described as follows:

(1) The property of FAST is changed from "PROGRAM" to "SUBROUTINE" after being called to examine the aero-servo-elastic simulation of the wind turbine.

(2) Subroutine "TimeMarch" is modified to specify the integration time and to remove the termination judgment.

(3) Subroutine "Gauss" that is the subroutine for solving Eq. (3) is modified to exclude the solutions of the platform's DOFs, since the platform kinematics including acceleration are calculated in the AQWA program and they will be used in the ElastDyn module.

(4) Subroutine "Solver" is modified to assign the platform kinematics based on the values transformed through the DLL for updating the kinematics of the upper structures.

(5) The tower-base loads are obtained from subroutine "CalcOuts" and then passed into the AQWA program after an appropriate coordinate transformation.

The key of F2A implementation is to consider the platform responses calculated in AQWA when examining the dynamics of the upper structures in FAST's subroutines. Therefore, steps (3)~(4) are the most crucial modifications for incorporating FAST to AQWA. It is noted that F2A has been released to the public. More specific implementation details of F2A can be found in GitHub via the link: https://github.com/yang7857854/F2A. The modifications to FAST's source code are commented with a start of “Yang”.

3.4 Validation

The F2A coupling framework is validated through comparisons with OpenFAST. The multi-body platform is modelled as a unibody concept by setting the tendons as rigid connections to be consistent with the modelling in OpenFAST. Dynamic responses of the FOWT under different wind-wave combinations obtained using F2A and OpenFAST are compared in the subsequent sections.

3.4.1 Steady wind and regular wave conditions

The design load cases (DLCs) defined in Table 2 are examined to verify the accuracy of F2A in evaluating coupled platform responses of the FOWT. The wind speed is assumed to be a constant for each DLC and the regular waves are generated using the Airy wave theory. Each of the simulations has a duration of 1500 s and a time step of 0.005 s. The statistical responses presented below are evaluated based on the results between 500 s and 1500 s.

Table 2: DLCs for the validation of steady wind and regular wave conditions[20]

ID of DLCs	Wind Speed (m/s)	Wave height (m)	Wave period (s)
1	4.0	1.6146	3.4985
2	6.0	1.6660	3.7746
3	8.0	1.8037	4.2657
4	10.0	2.0125	4.8954
5	12.0	2.2237	5.5570
6	14.0	2.4570	6.3366
7	16.0	2.6588	6.8895
8	18.0	2.9585	7.1203
9	20.0	3.1547	7.4570
10	22.0	3.4587	8.0225
11	24.0	3.8975	8.5650

Fig. 7 presents the mean values of platform motions and fairlead tension of mooring line #1 predicted by OpenFAST and F2A. It is observed that the dynamic responses of the FOWT predicted using F2A agree well with the results obtained using OpenFAST for each examined DLC. This implies that F2A is effective to predict coupled responses of the FOWT within its operation wind speed range.

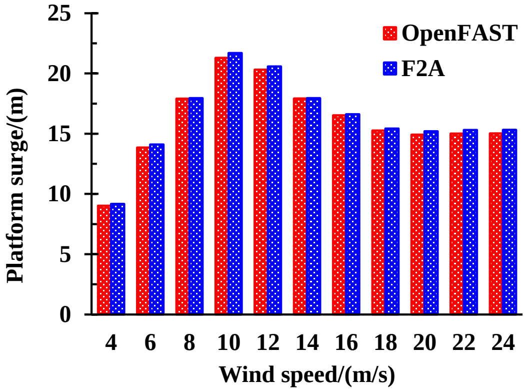

(a) Platform surge

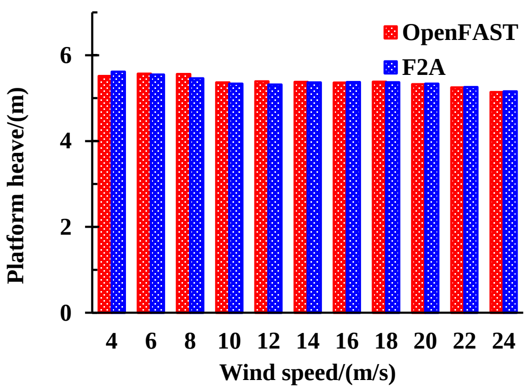

(b) Platform heave

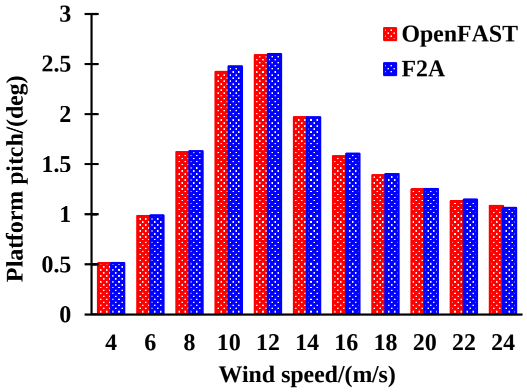

(c) Platform pitch

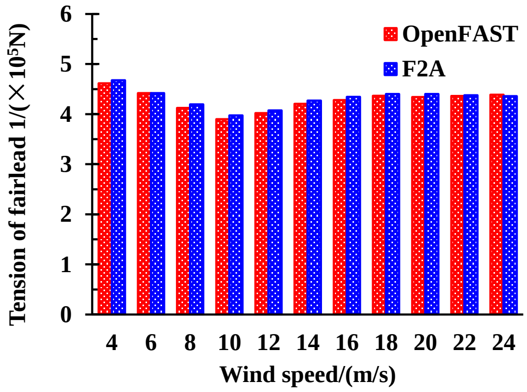

(d) Tension fairlead 1

Fig. 7: Comparison between OpenFAST and F2A for steady wind and regular wave conditions

3.4.2 Turbulent wind and regular wave condition

The turbulent wind condition is examined to further validate the accuracy of F2A for performing coupled analysis of FOWTs. Fig. 8 presents the rotor thrust, generator power and blade-tip deflection (out-of-plane) obtained using F2A and OpenFAST. The examined turbulent wind has an average speed of 11.4 m/s. The turbulence level of the wind is around 18.2%. The wave height and period of the examined regular wave condition are 2.22 m and 5.56 s, respectively. It is observed that the rotor thrust obtained by F2A agrees well with the predictions from OpenFAST, although slight difference in magnitude exists. The predictions of the generator power calculated by F2A and OpenFAST are almost identical. The same phenomenon is observed for the blade-tip deflection. These results indicate that the aerodynamic load prediction, servo-control and aeroelastic simulation capabilities have been successfully implemented within AQWA.

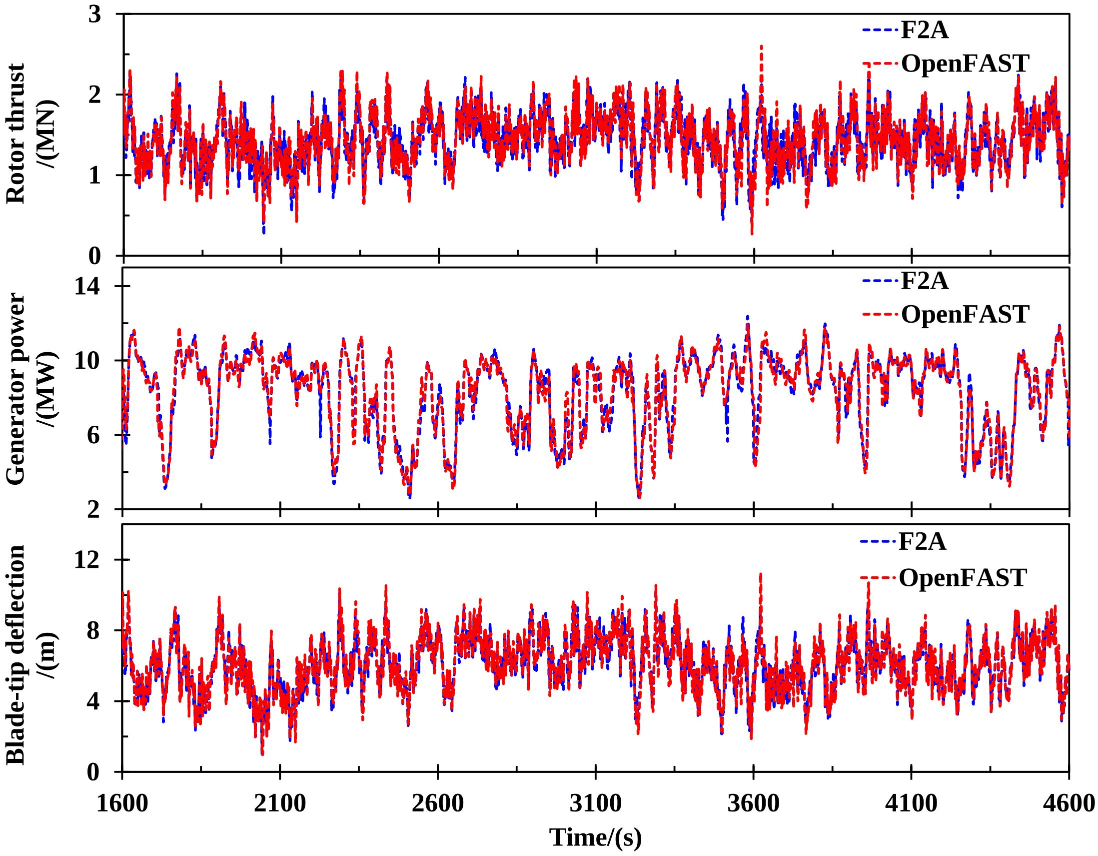

Fig. 8: Comparison of F2A against OpenFAST for aero-servo-elastic responses

Fig. 9 presents the coupled platform motions predicted by F2A and OpenFAST. It is found that the platform motions predicted by F2A agree well with the results from OpenFAST. The surge motions calculated in these two tools are almost identical. The pitch motion obtained by F2A is slightly larger than the predictions from OpenFAST. The difference is attributed to two aspects.

One of the reasons is the prediction of hydrodynamic load on the mooring lines. In OpenFAST, the hydrodynamic loads on the mooring lines are calculated based on the initial position of the platform in OpenFAST. However, the hydrodynamic loads on the mooring lines are predicted based on the instantaneous position of the platform in F2A. This implies that the wave kinematics used for the hydrodynamic load prediction in OpenFAST and F2A are different. This difference between OpenFAST and F2A is anticipated to produce discrepancies in the mooring tensions, leading to difference in platform motions.

The other reason is that the integration algorithms used for time-marching in OpenFAST and AQWA are different. In OpenFAST, the equation of the motion of the platform is solved in ElastDyn using the 4th-order Adams- Bashforth-Moulton predictor-corrector method. However, the platform motions are calculated in AQWA's solver using a 2nd-order predictor-corrector method.

Nonetheless, the overall agreements between F2A and OpenFAST regarding the predictions of platform responses are reasonably good.

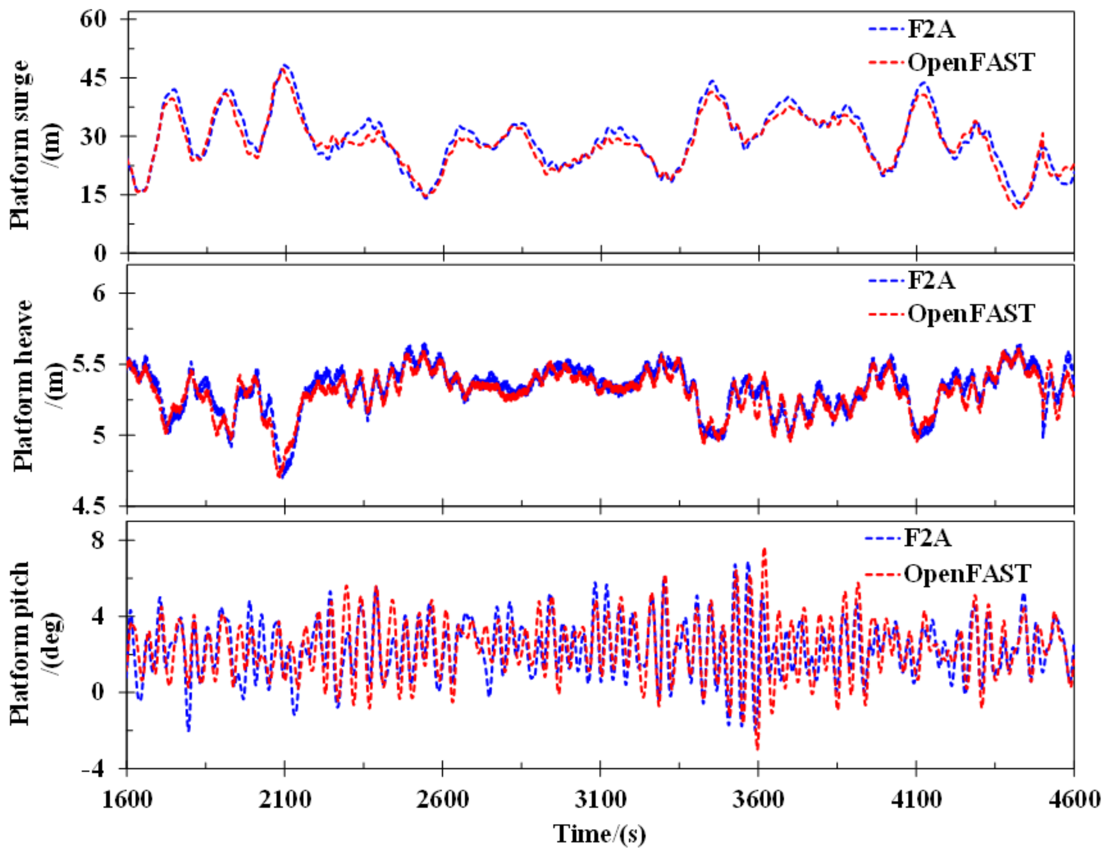

Fig. 9: Comparison of F2A against OpenFAST for platform responses

3.4.3 Turbulent wind and irregular wave condition

The platform responses of the FOWT due to a turbulent wind and an irregular wave are examined. The significant height and spectral peak period of the irregular wave are 3 m and 10 s, respectively. The average speed of the turbulent wind is 11.4 m/s. Fig. 10 presents the power spectral densities (PSDs) of platform motions obtained using F2A and OpenFAST. It can be observed that the PSDs from F2A have a peak frequency around 0.1 Hz and with magnitude similar to the results of OpenFAST for each motion signal. The spectral responses of F2A and OpenFAST agree with each other well. This has confirmed that F2A is capable of characterizing dynamic responses of the FOWT subjected to turbulent wind and irregular wave loadings.

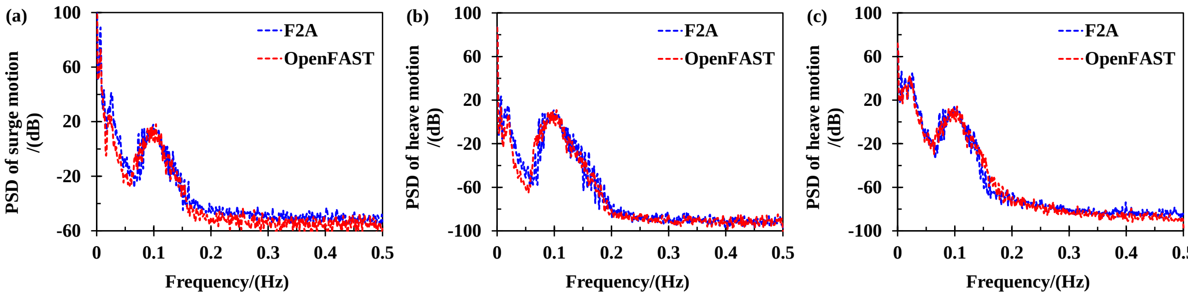

Fig. 10: PSDs of the platform motions due to irregular wave and turbulent wind. (a) Surge; (b) Heave; (c) Pitch.

4 Environmental conditions

The 10 MW TELWIND FOWT is expected to be installed in Atlantic deep-sea areas. According to the met-ocean data measured from 2011 to 2016 [27] for a specific site off the northern coast of Scotland, three typical environmental conditions (ECs) are defined as shown in Table 3.

Table 3: Definitions of the load cases

	Wind speed (m/s)	Significant wave height (m)	Spectral peak period (s)	Current speed at MSL (m/s)
EC 1	8.0	1.8	4.3	0.16
EC 2	11.4	2.2	5.6	0.22
EC 3	24.0	3.2	7.5	0.35

Since the distribution of the tendons is symmetrical, tendon breakage effects are examined for tendons #1, #2 and #3, respectively, under each EC given in Table 2. For a tendon failure scenario, the stiffness of the examined tendon will be zero from the failure occurrence time that is chosen as 3000 s, allowing for complete attenuation of initial transient behavior. Each simulation has a total duration of 4600 s and a time step of 0.005 s.

The inflow direction of wind aligns with the direction of wave and current loadings. TurbSim [28] is used to generate the corresponding turbulent winds based on the Kaimal spectrum. The vertical shear effect of the inflow wind is considered using a power law profile with an exponent of 0.12. The kinematics of the irregular wave are calculated using Airy wave theory. The vertical distribution of the current velocity is profiled in a power law formulation with an exponent of 1/7.

5 Results and discussions

5.1 Coupling effects under tendon breakage scenarios

The coupling effects of wind-wave loadings are investigated to confirm the necessity of using the fully coupled method for the tendon breakage analysis. The platform motions and tendon tensions are calculated using the coupled method (F2A) and a decoupled method. In the decoupled method, the aerodynamic loads are independent of platform motions. Fig. 11 presents the UT's motions obtained using the coupled and decoupled methods when tendon #1 is broken at 3000th s.

It is observed that the coupling effects between wind and wave loadings have a significant influence on the UT's motions. The surge and heave motions are comparatively insensitive to the coupling effects as confirmed by the minor differences between the results obtained using the decoupled and coupled methods. However, certain discrepancies exist in the pitch and yaw motions obtained through the decoupled and coupled methods. The pitch motion of the UT is significantly underestimated when the coupling effects are ignored. The same phenomenon is observed for the yaw motion, especially when a tendon breakage occurs. The coupling between the aerodynamic loads and platform motions leads to larger fluctuations in loads and responses. Following the breakage of tendon #1, the UT's yaw motion predicted using the coupled method varies in a much larger range compared to the result obtained by the decoupled method. These results have indicated that a decoupled method is incapable of appropriately predicting dynamic responses of the FOWT subjected to a tendon breakage.

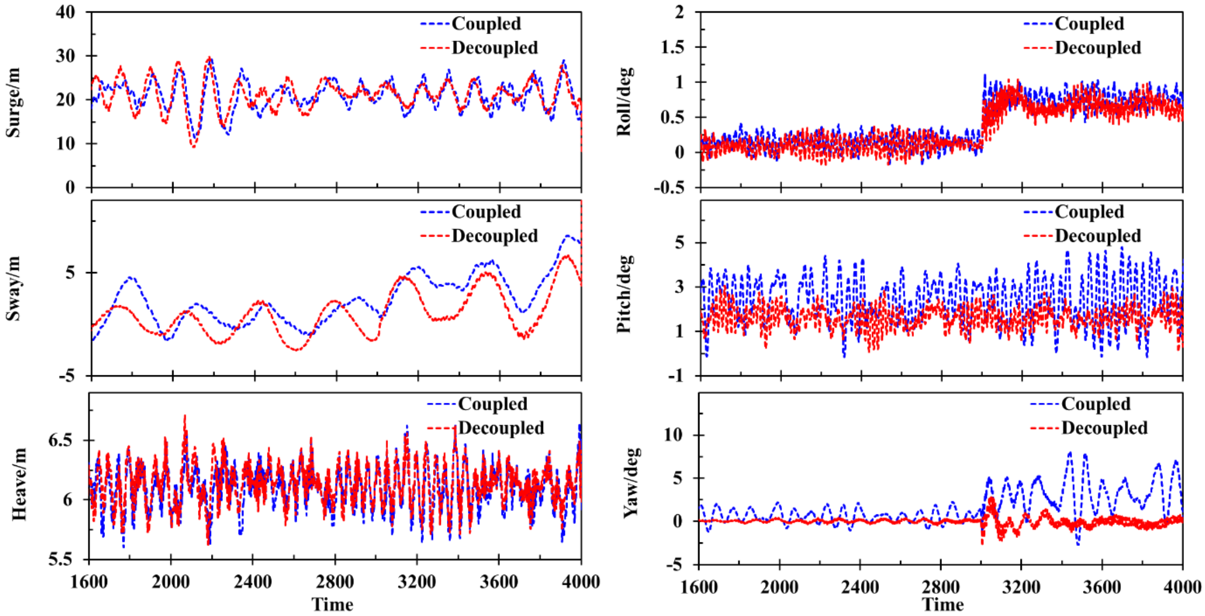

Fig. 11: UT's motions obtained using the coupled and decoupled methods

Fig. 12 presents the time series of tendon tensions and the statistical results obtained using the decoupled and coupled methods. It is found that the coupling effects have a notable influence on the tension in the tendons. The difference between the maximum or mean tendon tensions of these two methods is minor. However, the tension fluctuation predicted by the decoupled method is more severe than that obtained using the coupled method. This is because the tendon tensions are mainly determined by the relative motion difference between the UT and LT. In the decoupled method, the aerodynamic load is independent of the platform motions. As a result, the motion difference between the UT and LT could be larger compared to the coupled method in some circumstances. When the UT is moving against the wind due to the reduction of aerodynamic damping, the LT moves backward towards the UT. If the wind speed is lower than the rated wind speed, the coupling effect will result in a larger relative wind speed. As the aerodynamic load increases, the UT will be pushed forward to get close to the LT. However, in the decoupled model, the aerodynamic load will not increase due to the backward movement of the UT. The UT maintains its backward movement and the LT continues to follow UT. Therefore, the motion difference between the tanks in the coupled model is smaller than in the decoupled model. Consequently, the fluctuation of tendon tensions is smaller as observed from Fig. 12. The notable difference between the results obtained using the decoupled and coupled methods indicates that the coupling effects of wind and wave loadings must be accounted in tendon breakage analysis of the multi-body FOWT.

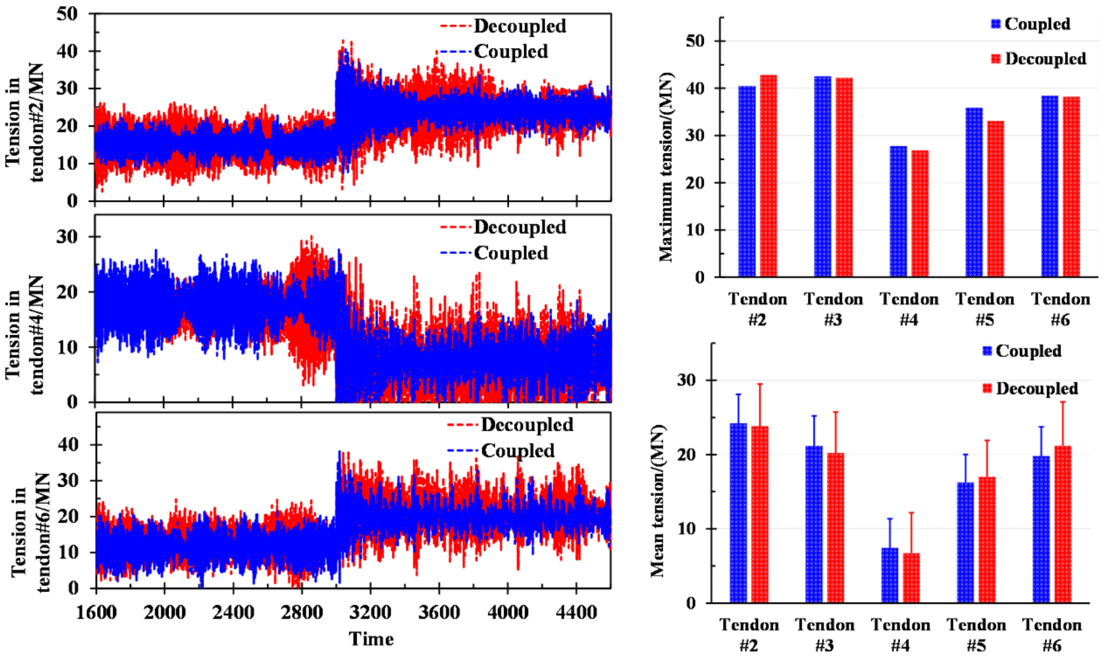

Fig. 12: Tension in the tendons obtained using the decoupled and coupled methods

5.2 Tendon breakage effects on the platform motions

For a tendon breakage situation, it is vital to obtain a good understanding on the variation of the platform's motions that directly indicate the stability of the wind turbine system.

The translation motions of the UT under tendon breakage scenarios are presented in Fig. 13. It is observed that the surge and heave motions are insensitive to a tendon breakage. This is because aerodynamic load that is mainly affected by the variation of turbulent wind is the dominant loading of the surge motion. The variation of platform surge velocity induced by a tendon breakage is relatively smaller than the wind speed variation. Thus, the aerodynamic load is not much affected by the tendon breakages. Conversely, sway motion is influenced by the tendon breakages, especially for the breakages of tendons #1 and #2 that are placed in the lateral side. The reduction of stiffness due to the tendon breakages leads to a larger sway motion of the UT. In the intact state, the maximum and mean values of the sway motion are 4.29 m and 0.81 m. After the breakage of tendon #1, the maximum sway is 8.77 m and the mean value is 3.8 m.

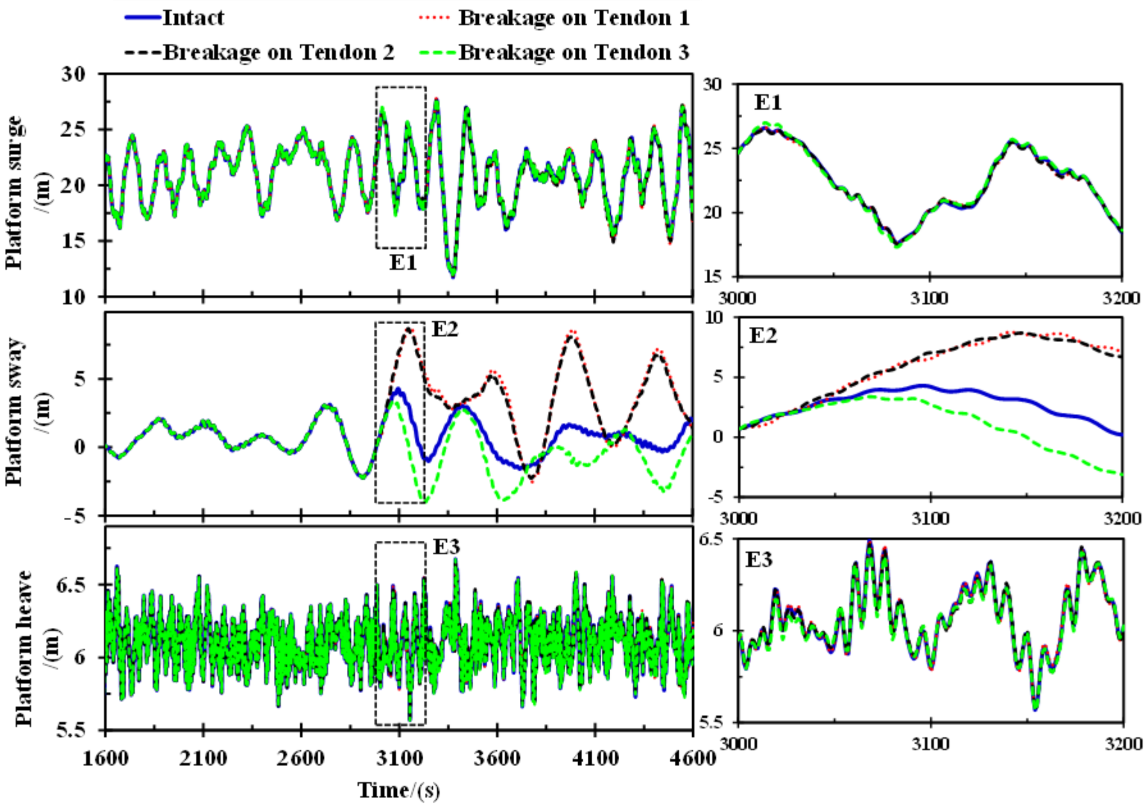

Fig. 13: Translational motions of the UT subjected to a failure on different tendons

Fig. 14 presents the rotational motions of the UT under tendon breakage scenarios. It is found that the roll and yaw motions vary around the zero magnitude with a small fluctuation before the occurrence of a tendon fracture. However, for each tendon breakage case, rotations of the UT fluctuate more severely with larger magnitudes after the fracture, especially for the roll and yaw motions. More specifically, a lateral inclination (roll) over 1.1 degrees is observed followed by the reduction in connection stiffness between the UT and LT after the failure of tendon #1, while the maximum roll is around 0.44 degrees on the intact condition. It is noted that the UT twists (yaw) to a magnitude of 9.2 degrees after a failure happened on tendon #1, while the maximum yaw of the intact condition is around 1.5 degrees. The pitch motion of the UT is comparatively insensitive to a tendon failure, although slight differences are observed between the results of different tendon failure scenarios. The average pitch motion increases from 2.4 degrees to 3.1 degrees after the breakage on tendon #3. Meanwhile, the maximum pitch motion increases from 3.8 degrees to 5.4 degrees.

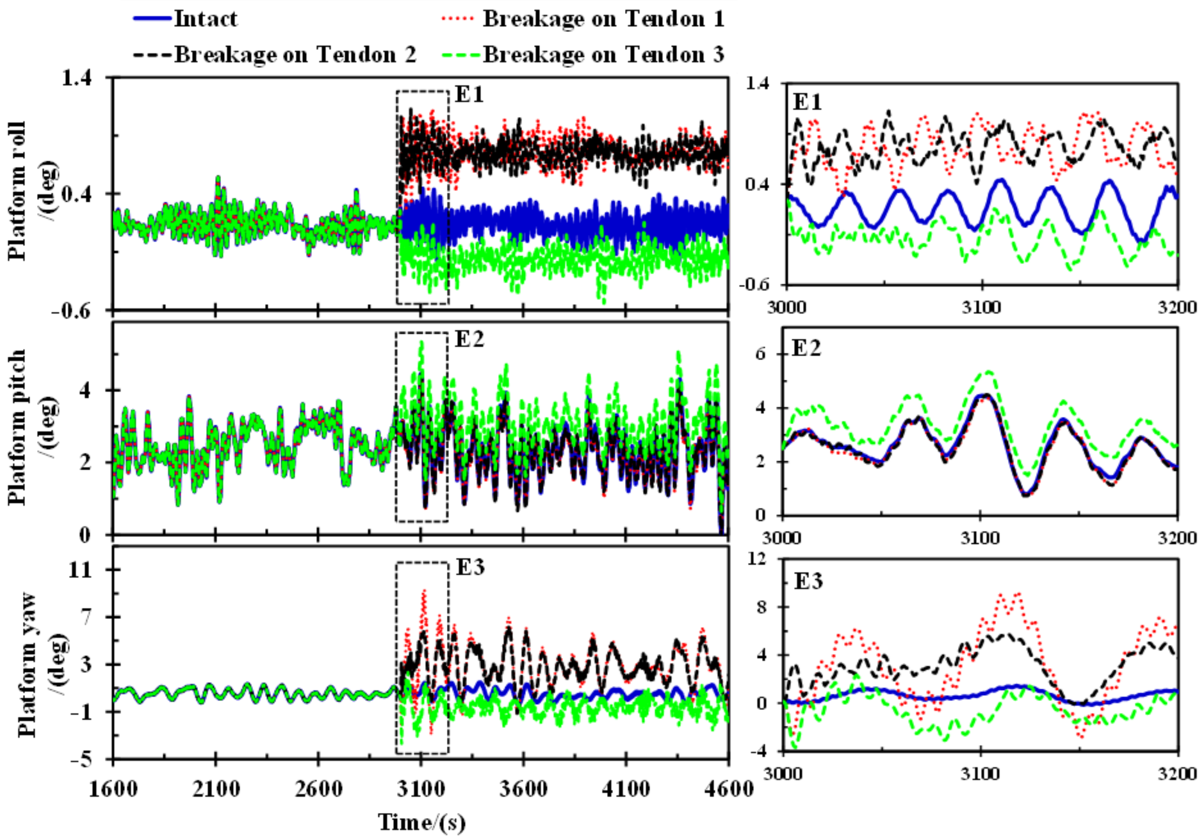

Fig. 14: Rotational motions of the UT subjected to a failure on different tendons

Fig. 15 presents the maximum rotational motions of the UT subjected to a tendon breakage under each examined EC. It is found that the maximum roll motion increases significantly due to the breakage of tendon #1 or tendon #2 for each examined EC. For EC 1 in which the wind speed is 8 m/s, the breakage of tendon #1 results in an increase in the roll motion by 516 %. With the increase of wind speed, the roll motion achieves larger maximum magnitude. The maximum roll is around 1.43 degrees when tendon #2 is broken suddenly under EC 3 in which the average wind speed is 24 m/s, which is close to the cut-out wind speed. It is noted that the maximum roll is still at a relatively small level even under the most severe condition when a tendon is subjected to a sudden failure. The results indicate that the whole wind turbine system will be stable in the roll DOF when a tendon fails in operational states.

As discussed previously, the pitch motion is relatively insensitive to a tendon breakage, although an enhancement on the maximum pitch motion is observed in the case of breakage on tendon #3. On EC 2, the breakage of tendon #3 produces a maximum pitch motion of 5.3 degrees which is 19.7% larger than that obtained from the intact condition. The maximum pitch motion of the UT of each examined load case is smaller than 6.0 degrees, implying that the wind turbine system does not have the risk of overturning when one of the tendons fails abruptly. It is found that a tendon breakage has significant effects on yaw motion of the UT. The breakage on tendon #1 leads to a relatively larger increase in the yaw motion compared to the failures of other two tendons. This means that breakage of a lateral tendon leads to a relatively larger loss in the yaw-stiffness of the particular platform.

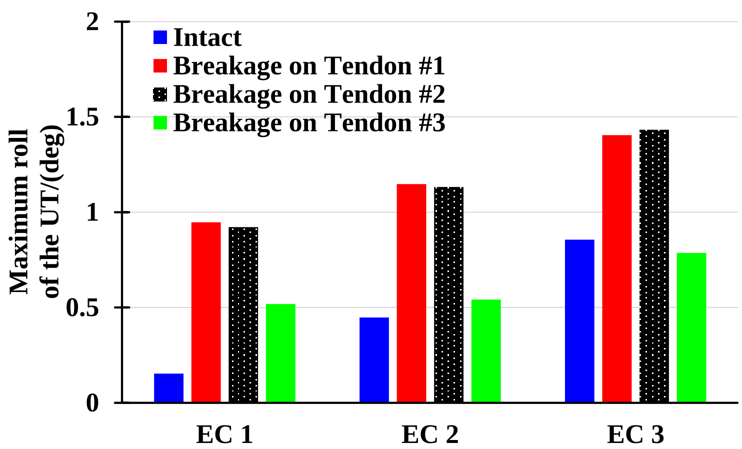

(a) Roll

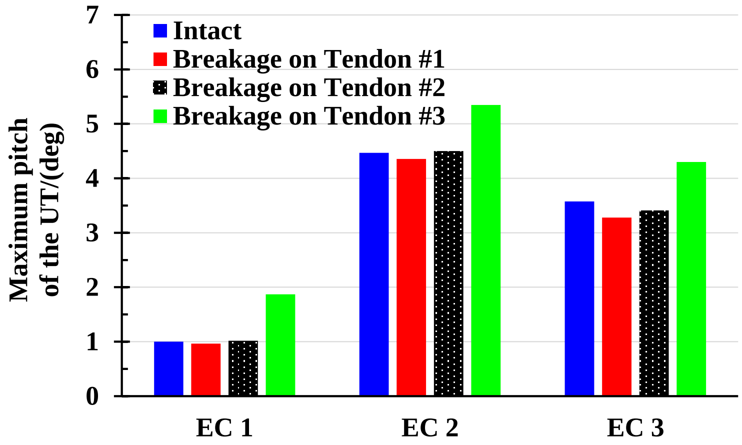

(b) Pitch

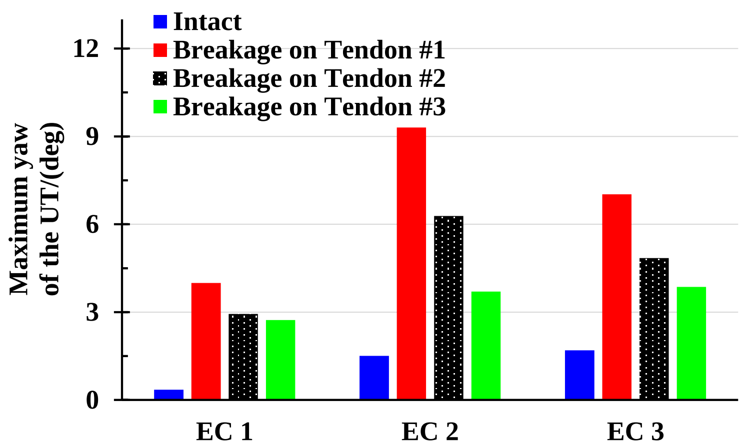

(c) Yaw

Fig. 15: Maximum rotational motions of the UT subjected to a tendon failure under each EC

The previous results have indicated that the breakage of tendon #1 produces a significant increase in the UT's motions. The remaining tendons are expected to experience larger tensions. Fig. 16 presents the tension in the tendons of the intact and tendon #1 breakage conditions. An abrupt tension variation is observed for each of the remaining tendons when tendon #1 is broken suddenly. Following the sudden variation in tension, tendon #1 was overstretched and subsequently breaks. The mean tension in tendon #2 and tendon #6 that are adjacent to tendon #1 is increased after the transient behaviour caused by the breakage. Conversely, tendon #4 behaves in an opposite manner to tendon #1 and is in a relatively looser state after the breakage of tendon #1. Consequently, the mean tension in tendon #4 is decreased. The mean tension in tendon #3 and tendon #5 remains in the same level as before tendon #1 is broken.

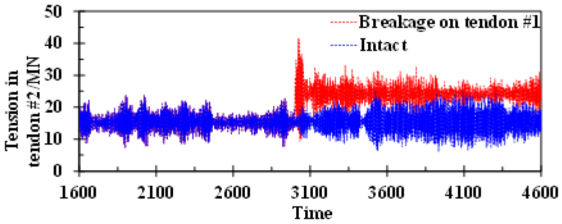

(a) Tendon #2

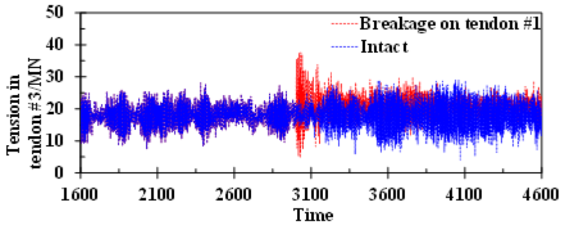

(b) Tendon #3

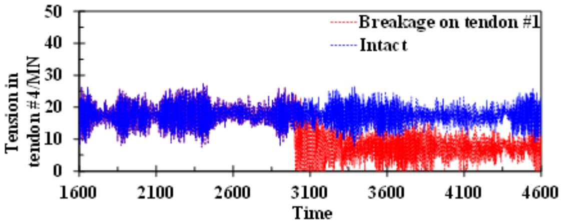

(c) Tendon #4

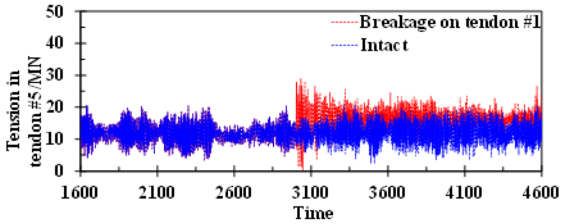

(d) Tendon #5

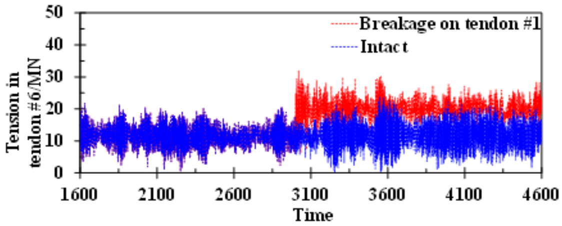

(e) Tendon #6

Fig. 16: Tension in the tendons under the intact and tendon #1 breakage conditions

Table 4 presents the statistical tension results of the remaining tendons under the intact and tendon #1 breakage conditions for the three ECs. It is found that tension in the remaining tendons with an exception of tendon #4 is increased for each EC. Under EC1, the standard deviation of tension in each tendon has a significant increase. This implies that the tendon breakage produces a relatively larger tension fluctuation.

The mean tensions in tendon #2 and tendon #6 that are adjacent to the broken tendon both increase by over 55% compared to the results of the intact state for each examined EC. The maximum tension in tendon #6 under EC3 that is the most severe wind-wave condition increases from 29.93 MN to 42.22 MN, equivalent to an increase of 41.1%. It is noted that maximum tension in tendon #4 is also increased by the tendon breakage under this EC while the peak tension is decreased. The results indicate that breakage leads to more severe transient behaviour under a harsh environmental condition. It is imperative to investigate the transient effects on tendon tensions under a tendon breakage scenario.

Table 4: Statistical tension in the remaining tendons under the intact and tendon #1 breakage conditions (Unit: MN)

		Tendon #2	Tendon #3	Tendon #4	Tendon #5	Tendon #6
EC1	Mean	14.96	15.51	15.41	14.13	14.09
		23.51	19.10	5.55	17.92	22.88
	Error	57.2%	23.2%	-64.0%	26.8%	62.4%
	Max	17.80	18.30	19.62	17.83	16.62
		29.27	26.04	13.55	23.87	27.48
	Error	64.5%	42.3%	-31.0%	33.9%	65.4%
	Std	0.83	0.91	0.89	0.95	0.74
		1.76	2.54	2.86	2.32	1.11
	Error	111.9%	179.3%	220.9%	145.5%	48.4%
EC2	Mean	15.31	17.78	17.40	12.03	11.75
		24.19	21.02	7.25	16.40	20.05
	Error	58.0%	18.2%	-58.3%	36.3%	70.6%
	Max	25.29	31.43	26.95	21.57	25.85
		33.93	31.74	21.31	27.27	32.17
	Error	34.2%	1.0%	-21.0%	26.4%	24.5%
	Std	3.88	4.74	3.18	3.50	4.59
		2.57	3.34	3.88	3.07	2.83
	Error	-33.8%	-29.6%	22.3%	-12.3%	-38.4%
EC3	Mean	15.22	16.38	16.16	13.27	13.14
		23.98	19.80	6.18	17.28	21.77
	Error	57.5%	20.9%	-61.7%	30.2%	65.7%
	Max	25.64	32.09	25.80	23.48	29.93
		37.69	33.68	28.49	36.32	42.22
	Error	47.0%	4.9%	10.4%	54.7%	41.1%
	Std	3.67	4.77	2.83	3.29	4.46
		3.71	4.11	4.72	4.25	4.49
	Error	0.9%	-14.0%	67.0%	29.1%	0.7%

5.3 Transient effects on the tendon tension

It is anticipated that tension in the adjacent tendon of the broken tendon would experience a tremendous increase due to the enhanced transient platform behavior. In order to obtain a good understanding of the transient effects on the tension variation, an additional load case is simulated for the scenario without a tendon in the first place.

Fig. 17 presents the tension in the adjacent tendon for each examined tendon breakage case under EC2. It is found that the tension in the adjacent tendon significantly increases following the tendon breakage. The sudden breakage produces a much larger tension in the adjacent tendon due to the transient effects. For instance, the maximum tension in tendon #2 is around 25.1 MN for the scenario with an intact tendon #1. The tension in tendon #2 achieve its maximum value of 41.5 MN at 22 seconds later than the sudden breakage on tendon #1. However, the tension is around 28.9 MN if tendon #1 is disconnected from the first place. This means that the transient effects result in a larger tension in tendon #2 by 43.6% when a failure happens on tendon #1. The most severe situation is the scenario of breakage on tendon #3. The maximum tension in tendon #4 after the breakage of tendon #3 is 50.3 MN that is less than half of its breaking load. In addition, the transient effects would dissipate within 100 seconds and the tension after the tendon breakage is lower than the peak tension in the transient duration. These mean that the remaining tendons are still at a safe condition without risking breakage. The tendons of the multi-body platform would not break one by one even if a breakage happens on one of the tendons.

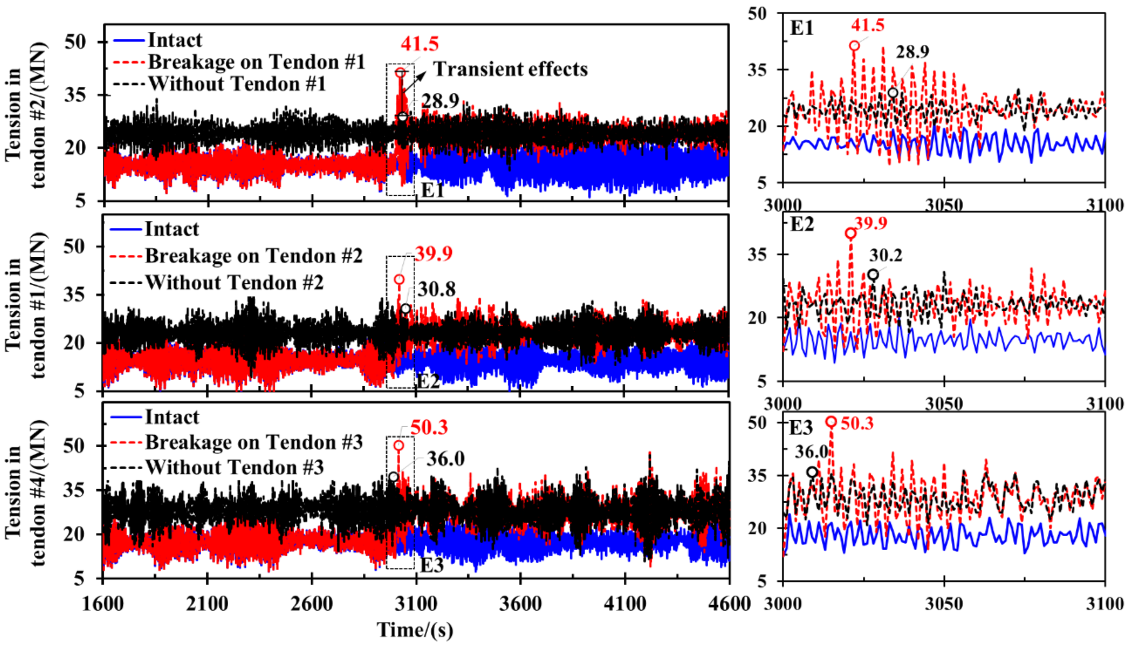

Fig. 17: Tension of the adjacent tendon when a tendon in failure under EC2

It can be concluded that the breakage of tendon #3 brings the most severe load to its adjacent tendon, *i.e.* tendon #4. The statistics of the tension in tendon #4 under all the examined ECs are presented in Fig. 18. The average tension under the sudden breakage scenario is close to that of the case without tendon #3 for all three ECs. However, a larger standard deviation is caused, especially for EC3 in which the wind speed is 24 m/s. The standard deviation of tension increases from 3.7 MN to 10.7 MN. It means that the resilience of the platform is weaker at higher wind speed conditions. The transient effects have a relative larger influence on a high wind speed condition. Fig. 12(b) indicates that the absence of tendon #3 leads to a heavier load in its adjacent tendon (#4) for all the examined ECs. In EC2, the maximum tension in tendon #4 of the intact state is 27.0 MN, while the maximum tension is 50.3 MN when the transient effect of the tendon breakage is considered. The tension increase in tendon #4 is more sensitive to the breakage under EC3 in which the wind speed is 24 m/s. The tension is increased from 25.8 MN to 68.4 MN, corresponding to an increase of 165.1%. However, this value did not reach 60% of the breaking load of the tendon, implying that the tendon is still in a safe state.

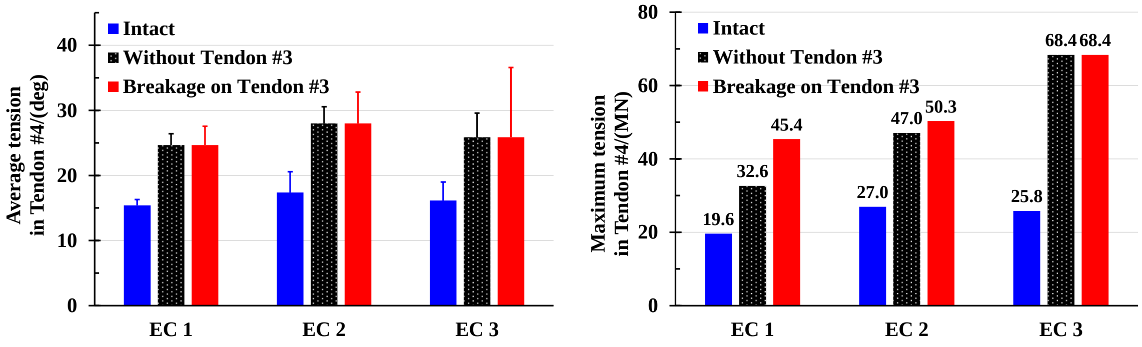

(a) Mean value (b) Maximum value

Fig. 18: Statistics of tension in tendon #4 under all the ECs

5.4 Spectral characteristics of tendon breakage

The Welch transformation and the wavelet leader approaches are used to obtain the spectral responses of the platform subjected to tendon breakages, which is beneficial to the development of structural health monitoring system for the identification and detection of a tendon damage.

5.4.1 Welch transformation

The breakage of a tendon would produce a loss of connection stiffness between the UT and LT, leading to a change in the vibration modes of the platform. As a result, the spectral characteristics of the platform responses under a tendon breakage scenario are anticipated to be different from those on the intact state.

Fig. 19 presents the spectral responses of the UT by applying the Welch transformation on its acceleration time series. It is found that the wave excitation is the major contributor to the surge response of the platform. When the breakage occurs on tendon #3, the spectral response corresponding to the wave excitation is slightly reduced compared to the results of the intact state. The breakage of tendon #2 does not reduce the contribution of wave excitation to the surge response. Apart from the wave excitation, the collective-pitch, local-pitch and coupled-pitch modes of the platform are activated. The contribution of the collective-pitch mode is insensitive to a tendon breakage. In contrast, the local-pitch and coupled pitch modes are significantly affected by a tendon breakage. When tendon #2 is broken, the contribution of the local pitch mode to the UT's responses is smaller. This is because the coupled-pitch mode contributes more to the UT's responses. It means that the UT also vibrates in a relatively large amplitude that is similar to the LT, as described in Table 1. Due to the stiffness reduction, the frequency of the coupled-pitch mode is decreased from 0.68 Hz to 0.55 Hz. For the breakage of tendon #3, changes in the spectral response at the local-pitch mode frequency are insignificant. However, the frequency of the coupled-pitch mode is heavily reduced and the spectral response is significantly enhanced.

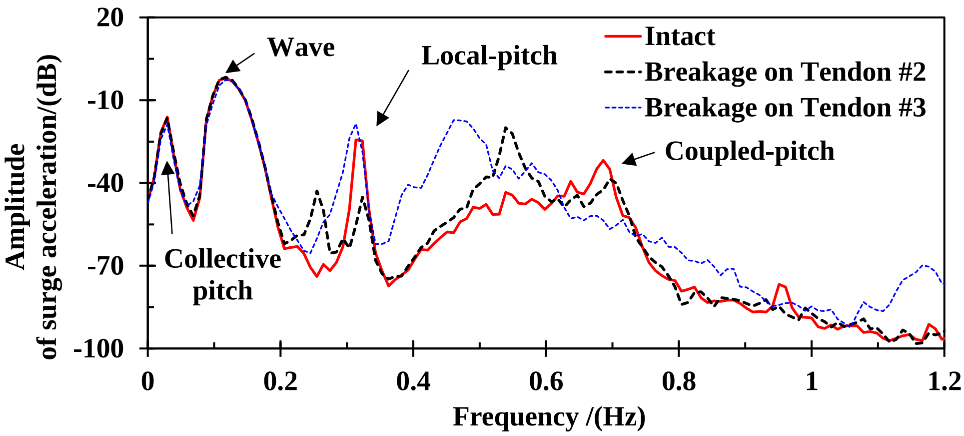

(a) Surge acceleration

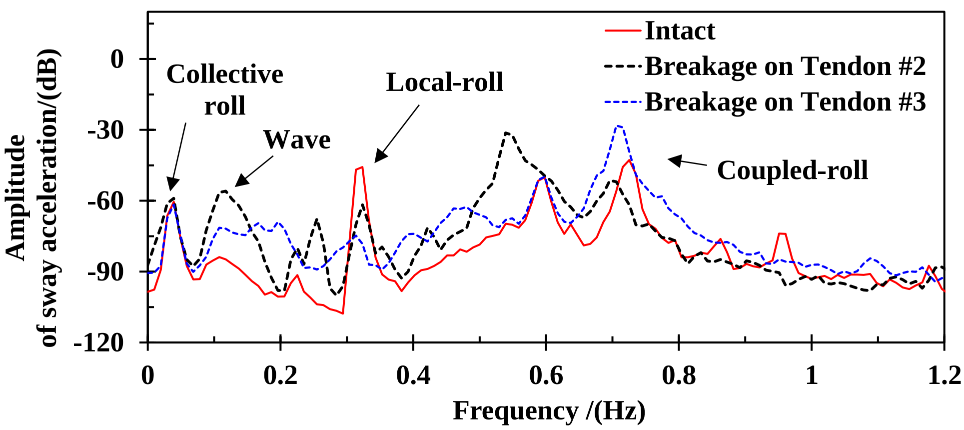

(b) Sway acceleration

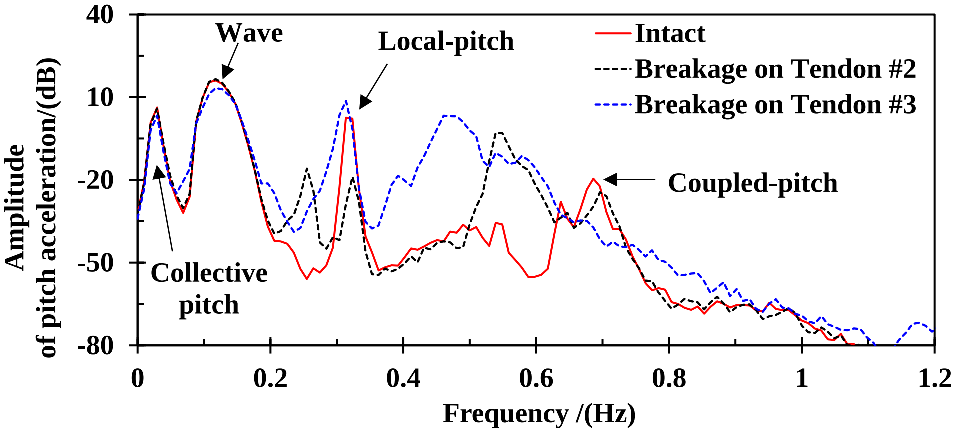

(c) Pitch acceleration

Fig. 19: Welch-based spectral responses of the UT under EC2

It is found from Fig. 19(b) that the local-roll mode is suppressed due to a tendon breakage, while the wave excitation contribution is increased. The spectral responses corresponding to the coupled-roll mode are increased by a tendon breakage, but in a smaller frequency. As presented in Fig. 19(c), the collective-pitch mode is the major contribution to the pitch acceleration of the UT. In addition, the similar amplitudes of different tendon breakage scenarios at the collective-pitch frequency have confirmed again that the collective-pitch mode is not affected by a tendon breakage. Similar to the surge acceleration, the local-pitch and coupled-pitch modes are more sensitive to a tendon loss, especially the coupled-pitch mode. The spectral response of the coupled-pitch of a tendon breakage scenario achieves a larger peak at a smaller frequency. The results presented in Fig. 13 imply that surge and pitch accelerations are sensitive to a tendon breakage. In addition, the wave excitation contributions on these two responses are not affected by the loss of a tendon. Therefore, these two signals are suitable for the identification of tendon damage.

5.4.2 Multifractal spectrum analysis

Apart from the Welch spectral responses that have certainly reflected the influence of a tendon breakage by showing the changes in vibration frequencies and amplitudes, multifractal spectrum analysis is another efficient method that shows the nonlinear characteristics of the platform responses. As presented in Fig. 20, multifractal spectrum [29] is a curve of the correlation between Hausdorff dimension (*D*) [30] and Hölder exponents (*H*) [31] which quantifies the multifractality of a signal.

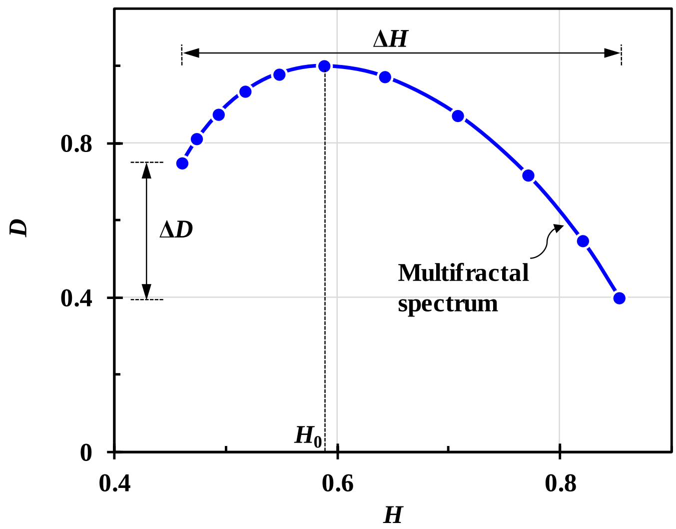

Fig. 20: A sample of multifractal spectrum

Hölder exponent is a parameter that describes the local regularity of a nonlinear curve at a specific point x_0. The curve at x_0 is differentiable if $H(x_0) < 1$. In this case, the exponent denotes the smoothness or otherwise of the curve at x_0, and it shows how spiky the curve is. For a nonlinear curve, the Hölder exponent changes from point to point. It is effective in extracting some inherent features of the signal by characterizing the set of points with the same pointwise regularity (*i.e.* the Hölder exponent).

Hausdorff dimension [32] is the oldest definition of fractal dimension which presents the best analytical property of a naturally occurring irregular graph. For instance, the Hausdorff dimension is one for a straight line and is three for a cube. This dimension is an extended non-negative real number associated with a metric space and it was developed by Hausdorff in 1919 to define measures by means of coverings of certain subsets. For a metric space (X,ρ) and a positive real number δ, the diameter of any subset A of X is defined, as usual, by $\mathrm{diam}(A)=\sup\{\rho(x,y);x,y\in A\}$. The countable family of subsets $\{U_i\}_{i\in I}$ is δ-cover of a subset $F\subset X$, if $F\subseteq\bigcup_{i\in I}U_i$ with $\mathrm{diam}(U_i)\leq\delta$ for all $i\in I$. The class of all δ-covers of F is denoted by $C_\delta(F)$. Then, the so-called s-dimensional Hausdorff measure of F is defined as follows:

$$H_H^s(F)=\lim_{\delta\to 0}\left(\inf\left\{\sum_{i\in I}diam(U_i)^s:\{U_i\}_{i\in I}\in C_\delta(F)\right\}\right) \tag{13}$$

$H_H^s(F)$ generalizes the classical Lebesgue measure for Euclidean subspaces. Therefore, the Hausdorff dimension of F, $D(F)$, as the point s where $H_H^s(F)$ "jumps" from ∞ to 0, namely,

$$D(F)=\inf\{s:H_H^s(F)=0\}=\sup\{s:H_H^s(F)=\infty\} \tag{14}$$

The multifractal spectrum of a signal is the distribution of the Hausdorff dimensions corresponding to different sets of points with the same pointwise regularity (*i.e.* the Hölder exponent). Similarly, the multifractal spectrum provides a measure of how much the local regularity of a signal varies in time. In general, the width (ΔH see Fig. 20) of a multifractal spectrum reflects the fluctuation intensity of the signal. A signal exhibits essentially the same regularity everywhere in time and therefore has a multifractal spectrum with a small width. Conversely, the multifractal spectrum with a larger width implies that the signal exhibits variations in signal regularity over time.

The difference (ΔD) between the Hausdorff dimensions at the maximum and minimum Hölder exponents denotes the local intensity of the signal. H_0 is the Hölder exponent corresponding to the maximum Hausdorff dimension. The value of H_0 is used to determine whether the signal is anti-persistent or persistent. For a signal with H_0 smaller than 0.5, the signal is anti-persistent and exhibits a short memory. The time series tends to always revert to its mean value, implying that the system behavior is unstable. When H_0 is larger than 0.5, the signal is persistent and has a relatively long memory. In a persistent signal, increases in value tend to be followed by subsequent increases. It is very useful to determine that the signal is anti-persistent or persistent for prediction in future.

It is accepted that multifractal spectrum is able to quantitatively describe the internal nonlinearity and self-similarity of a complex signal by dividing the signal into smaller sets with different singularities [33-38]. Therefore, the multifractal spectrum analysis method is used to identify features of tendon damage.

Using the wavelet leader approach described in [39-41], multifractal spectra of the UT's accelerations subjected to a tendon breakage under EC2 are obtained as presented in Fig. 21. It is apparent that the H_0 of tendon failure scenarios is smaller than that of the intact state. As revealed previously, breakage of tendon #3 has a relatively larger influence on surge motion of the UT. As a result, the corresponding H_0 is the smallest. In other words, the Hausdorff dimension achieves its peak at the smallest Hölder exponent. This phenomenon is also observed from the multifractal spectra of the UT's heave and pitch accelerations. The results have confirmed that the multifractal spectrum of the surge acceleration signal can identify a tendon failure effectively.

672 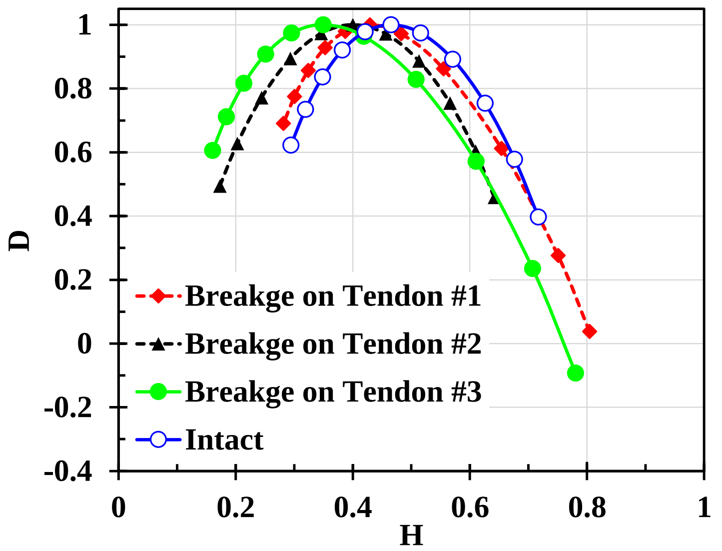

673 (a) Surge

674 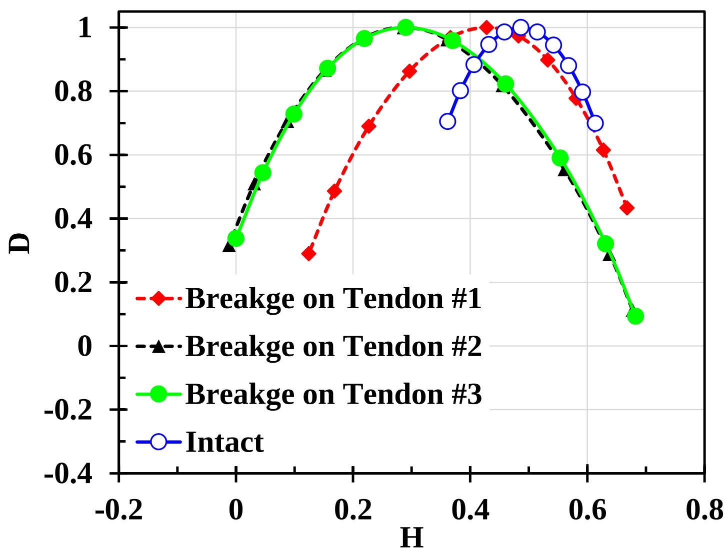

675 (b) Heave

676 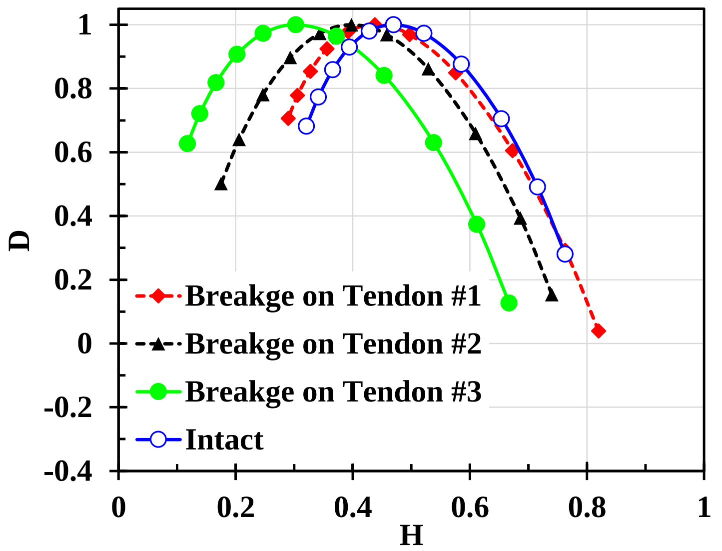

(c) Pitch

Fig. 21: Multifractal spectra of UT's accelerations under EC2

As observed in Fig. 21(b), the magnitudes of H_0 of the multifractal spectra are close to each other when the breakage happens on tendon #2 or #3. The value is also smaller than that of the spectrum when a failure occurs on tendon #1. In addition, the width of a multifractal spectrum of a tendon failure scenario is close to each other and is much larger than that of the intact state. This means that the fluctuation intensity of heave acceleration subjected to a tendon failure is larger than that of the intact state. In addition, the tendon breakage location has a weak influence on the fluctuation intensity of the UT's heave acceleration. This means that heave acceleration signal is not effective enough for the damage localization. However, the value of H_0 of each multifractal spectrum of the pitch acceleration is different from each other. Therefore, the pitch acceleration is suitable for localizing tendon breakages.

6 Conclusions

This study investigates the dynamic behaviors of a 10 MW wind turbine supported by a coupled two-body floating platform under different tendon failure scenarios. In order to examine the fully coupled aero-hydro-servo-elastic effects of the FOWT, a newly-developed coupling framework (F2A), which is based on AQWA and FAST, is used. The time-domain dynamic responses of the platform subjected to different tendon failures are calculated and analyzed. Using the Welch-based technique and multifractal spectrum analysis approach, spectral characteristics of the platform responses are obtained to identify effective features of tendon failures. The conclusions from the study are given as follows:

(1) Dynamic behaviors of the multi-body floating platform heavily depend upon the integrity of the tendons. It is found that the roll and yaw motions of the UT could be enhanced by six times when a tendon failure occurs. The platform pitch motion is relatively insensitive to a tendon breakage.

(2) The tension in the tendon adjacent to the broken tendon increases significantly following the tendon breakage. The breakage of the tendon that aligns with the wind direction leads to the most severe loads in the remaining tendons. An increase of 165.1% in tension of its adjacent tendon is produced for the examined over-rated condition. The transient effects due to a tendon breakage increases the tension fluctuation in the adjacent tendon.

(3) Tendon breakages have weak effects on the wave excitation and collective-pitch mode, which are the main contributors to the platform surge and pitch fluctuations. However, a tendon breakage enhances the spectral responses corresponding to the coupled-pitch mode. The surge and pitch acceleration signals of the UT can be used to identify a tendon damage.

(4) Multifractal spectra of the platform acceleration signals obtained from the simulations under different tendon failure scenarios show distinct fractal characteristics. The Hausdorff dimension of the multifractal spectra under failure scenarios achieves its peak at a smaller Hölder exponent compared to the healthy state. Tendon failures is easily detected using the multifractal spectrum analysis approach.

Acknowledgements

This project is funded by European Regional Development Fund (ERDF), Interreg Atlantic Area (grant number: EAPA_344/2016) and Shanghai Pujiang Program (2019PJD054). The authors would like to acknowledge the financial supports from the European Union's Horizon 2020 research and innovation programme under the Marie Skłodowska-Curie grant agreement no. 730888 (RESET), Royal Society (grant number: IEC\NSFC\170054), the National Natural Science Foundation of China (grant numbers: 51976131) and Science and Technology Commission of Shanghai Municipality (grant number: 1906052200).

References

[1] GWEC. Global wind report 2019. Global Wind Energy Council, Brussels: 2020.

[2] Yang, Y., Bashir, M., Li, C., & Wang, J. (2019). Analysis of seismic behaviour of an offshore wind turbine with a flexible foundation. Ocean Engineering, 178, 215-228.

[3] Bak, C., Bitsche, R., Yde, A., Kim, T., Hansen, M. H., Zahle, F., ... & Behrens, T. (2012). Light Rotor: The 10-MW reference wind turbine. In EWEA 2012-European Wind Energy Conference & Exhibition. European Wind Energy Association (EWEA).

[4] Velarde, J. (2016). Design of monopile foundations to support the DTU 10 MW offshore wind turbine (Master's thesis, NTNU).

[5] Velarde, J., & Bachynski, E. E. (2017). Design and fatigue analysis of monopile foundations to support the DTU 10 MW offshore wind turbine. Energy Procedia, 137, 3-13.

[6] Azcona, J., F. Vittori, U. Schmidt, F. Svanije, G. Kapogiannis, X. Karvelas, D. Manolas. (2017). Design Solutions for 10 MW Floating Offshore Wind Turbines. INNWIND. EU, Deliverable D 4: 37.

[7] Yu, W., K. Müller, F. Lemmer, H. Bredmose, M. Borg, G. Sanchez, and T. Landbo. (2017). Public Definition of the Two LIFES50+ 10MW Floater Concepts." LIFES50+ Deliverable 4.

[8] Armesto, J. A., Jurado, A., Guanche, R., Couñago, B., Urbano, J., & Serna, J. (2018, June). Telwind: Numerical analysis of a floating wind turbine supported by a two bodies platform. In ASME 2018 37th International Conference on Ocean, Offshore and Arctic Engineering. American Society of Mechanical Engineers Digital Collection.

[9] Gao, Z., & Moan, T. (2007). Sensitivity study of extreme value and fatigue damage of line tension in mooring system with one line failure under varying annual environmental conditions. *The Seventeenth International Offshore and Polar Engineering Conference, International Society of Offshore and Polar Engineers*, Hawaii, USA.

[10] Zhang, Z., Kim, M. H., & Ward, E. G. (2009). Progressive mooring-line failure of a deepwater MODU in hurricane conditions. *In ASME 2009 28th International Conference on Ocean, Offshore and Arctic Engineering, American Society of Mechanical Engineers*, Hawaii, USA.

[11] Yang, C. K., & Kim, M. H. (2010). Transient effects of tendon disconnection of a TLP by

hull–tendon–riser coupled dynamic analysis. *Ocean Engineering*, 37(8-9), 667-677.
[12] Kim, M. H., & Zhang, Z. (2009). Transient effects of tendon disconnection on the survivability of a TLP in moderate-strength hurricane condition. *International Journal of Naval Architecture and Ocean Engineering*, 1(1), 13-19.
[13] Yang, C. K., Padmanabhan, B., Murray, J., & Kim, M. H. (2008). The transient effect of tendon disconnection on the global motion of ETLP. *In ASME 2008 27th International Conference on Offshore Mechanics and Arctic Engineering. American Society of Mechanical Engineers*, Estoril, Portugal.
[14] Ahmed, M. O., Yenduri, A., & Kurian, V. J. (2016). Evaluation of the dynamic responses of truss spar platforms for various mooring configurations with damaged lines. *Ocean Engineering*, 123, 411-421.
[15] Malayjerdi, E., Ahmadi, A., & Tabeshpour, M. R. (2017). Dynamic Analysis of TLP in intact and damaged tendon conditions. *International Journal of Coastal & Offshore Engineering*,1, 23-33.
[16] Yu, J., Hao, S., Yu, Y., Chen, B., Cheng, S., & Wu, J. (2019). Mooring analysis for a whole TLP with TTRs under tendon one-time failure and progressive failure. *Ocean Engineering*, 182, 360-385.
[17] Bae, Y. H., Kim, M. H., & Kim, H. C. (2017). Performance changes of a floating offshore wind turbine with broken mooring line. *Renewable Energy*, 101, 364-375.
[18] Li, Y., Zhu, Q., Liu, L., & Tang, Y. (2018). Transient response of a SPAR-type floating offshore wind turbine with fractured mooring lines. *Renewable Energy*, 122, 576-588.
[19] Ma, G., Zhong, L., Zhang, X., Ma, Q., & Kang, H. S. (2020). Mechanism of mooring line breakage of floating offshore wind turbine under extreme coherent gust with direction change condition. *Journal of Marine Science and Technology*, 1-13.
[20] Yang, Y., Bashir, M., Michailides, C., Li, C., & Wang, J. (2020). Development and application of an aero-hydro-servo-elastic coupling framework for analysis of floating offshore wind turbines. *Renewable Energy*, 161, 606-625.
[21] Yang, Y., Bashir, M., Wang, J., Michailides, C., Loughney, S., Armin, M., ... & Li, C. (2020). Wind-wave coupling effects on the fatigue damage of tendons for a 10 MW multi-body floating wind turbine. *Ocean Engineering*, 217, 107909.
[22] Bak, Christian, Frederik Zahle, Robert Bitsche, Taeseong Kim, Anders Yde, Lars Christian Henriksen, Anand Natarajan, and Morten Hartvig Hansen. (2013). Description of the DTU 10 MW reference wind turbine. DTU Wind Energy Report-I-0092 5.
[23] Moriarty, P. J., & Hansen, A. C. (2005). AeroDyn theory manual (No. NREL/TP-500-36881). National Renewable Energy Lab., Golden, CO (US).
[24] Jonkman, J. M., Hayman, G. J., Jonkman, B. J., Damiani, R. R., & Murray, R. E. (2015). AeroDyn v15 User's Guide and Theory Manual. NREL: Golden, CO, USA.
[25] Yang, Y., Li, C., Zhang, W., Yang, J., Ye, Z., Miao, W., & Ye, K. (2016). A multi-objective optimization for HAWT blades design by considering structural strength. Journal of Mechanical Science and Technology, 30(8), 3693-3703.
[26] Peters, D. A., & He, C. J. (1991). Correlation of measured induced velocities with a

finite - state wake model. Journal of the American Helicopter Society, 36(3), 59-70.

[27] Ifremer. Marine Data Portal, French Research Institute for the Exploitation of the Sea, Online: http://data.ifremer.fr/pdmi/portalssearch/main. Data Accessed: January 2019.

[28] Jonkman, Bonnie J. (2009). TurbSim user's guide: Version 1.50. No. NREL/TP-500-46198. National Renewable Energy Lab.(NREL), Golden, CO (United States).

[29] Falconer, K. J. (1994). The multifractal spectrum of statistically self-similar measures. Journal of Theoretical Probability, 7(3), 681-702.

[30] Falconer, K. J. (1988, March). The Hausdorff dimension of self-affine fractals. In Mathematical Proceedings of the Cambridge Philosophical Society (Vol. 103, No. 2, pp. 339-350). Cambridge University Press.

[31] Kolwankar, K. M., & Gangal, A. D. (1997). Hölder exponents of irregular signals and local fractional derivatives. Pramana, 48(1), 49-68.

[32] M. Fernández-Martínez a, & M.A. Sánchez-Granero b. (2015). How to calculate the Hausdorff dimension using fractal structures. Applied Mathematics and Computation, 264, 116-131.

[33] Meneveau, C., & Sreenivasan, K. R. (1987). The multifractal spectrum of the dissipation field in turbulent flows. Nuclear Physics B-Proceedings Supplements, 2, 49-76.

[34] Ivanov, P. C., Amaral, L. A. N., Goldberger, A. L., Havlin, S., Rosenblum, M. G., Struzik, Z. R., & Stanley, H. E. (1999). Multifractality in human heartbeat dynamics. Nature, 399(6735), 461.

[35] Matia, K., Ashkenazy, Y., & Stanley, H. E. (2003). Multifractal properties of price fluctuations of stocks and commodities. EPL (Europhysics Letters), 61(3), 422.

[36] Yao, B., Imani, F., Sakpal, A. S., Reutzel, E. W., & Yang, H. (2018). Multifractal analysis of image profiles for the characterization and detection of defects in additive manufacturing. Journal of Manufacturing Science and Engineering, 140(3), 031014.

[37] Ebrahimkhanlou, A., Farhidzadeh, A., & Salamone, S. (2016). Multifractal analysis of crack patterns in reinforced concrete shear walls. Structural Health Monitoring, 15(1), 81-92.

[38] Carpinteri, A., Lacidogna, G., & Niccolini, G. (2009). Fractal analysis of damage detected in concrete structural elements under loading. Chaos, Solitons & Fractals, 42(4), 2047-2056.

[39] Lashermes, B., Jaffard, S., & Abry, P. (2005, March). Wavelet leader based multifractal analysis. In Proceedings of ICASSP'05. IEEE International Conference on Acoustics, Speech, and Signal Processing, 2005. (Vol. 4, pp. iv-161). IEEE.

[40] Jaffard, S., Lashermes, B., & Abry, P. (2006). Wavelet leaders in multifractal analysis. In Wavelet analysis and applications (pp. 201-246). Birkhäuser Basel.

[41] Wendt, H., Abry, P., Jaffard, S., Ji, H., & Shen, Z. (2009, November). Wavelet leader multifractal analysis for texture classification. In 2009 16th IEEE International Conference on Image Processing (ICIP) (pp. 3829-3832). IEEE.